



3 1293 01561 0904



This is to certify that the

thesis entitled

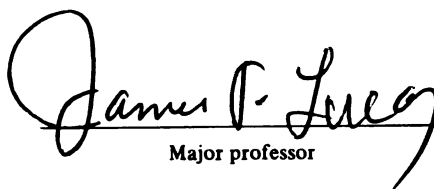
EFFECTS OF AGING ON FRACTURE BEHAVIOR IN Al MATRIX
PARTICULATE REINFORCED METAL MATRIX COMPOSITES

presented by

Jong-kook Park

has been accepted towards fulfillment
of the requirements for

M.S. degree in Materials Science


Major professor

Date Dec. 10, 1996

PLACE IN RETURN BOX to remove this checkout from your record.
TO AVOID FINES return on or before date due.

DATE DUE	DATE DUE	DATE DUE
_____	_____	_____
_____	_____	_____
_____	_____	_____
_____	_____	_____
_____	_____	_____
_____	_____	_____
_____	_____	_____

**EFFECTS OF AGING ON FRACTURE BEHAVIOR IN Al MATRIX
PARTICULATE REINFORCED METAL MATRIX COMPOSITES**

By

Jong-kook Park

A THESIS

Submitted to
Michigan State University
in partial fulfillment of the requirements
for the degree of

MASTER OF SCIENCE

Department of Materials Science and Mechanics

1996

ABSTRACT

EFFECTS OF AGING ON FRACTURE BEHAVIOR IN Al MATRIX PARTICULATE REINFORCED METAL MATRIX COMPOSITES

By

Jong-kook Park

Crack propagation behavior is investigated in relation to various interface microstructures evolved during solution heat treatment and artificial aging in 6061 aluminum based Al_2O_3 and SiC particulate reinforced metal matrix composites (PRMMCs). Materials investigated were extruded bars of Al_2O_3 /6061Al, and SiC/6061Al PRMMCs produced by a stir-cast melt process. Interface microstructure characterization and crack profile analyses were carried out using optical microscope with digital imaging capability. Scanning and transmission electron microscope were used to analyze microstructural details, such as interfacial composition, chemistry and fracture surface morphology. Examinations of SiC_p/6061Al composite interface, subjected to a moisture (H_2O) environment, was also conducted using environmental scanning electron microscope (ESEM) to ascertain the hydrophilic nature of the interface. Mechanical testing was conducted on double notched, 4-point-bend and short bar fracture toughness specimens in the under aged, peak aged, and over aged conditions. Interfacial microstructure that formed during solution heat treatment and artificial aging played a significant role on observed microfracture mechanisms in PRMMCs. Aging conditions, reinforcement type, and microstructural formation all influenced the crack growth processes, such as crack initiation, microcrack formation ahead of the crack tip, and microcracks/main crack link up mechanisms.

To my lovely wife and family

Acknowledgments

I would like to thank Prof. J. P. Lucas for his guidance, advice and financial support throughout the duration of this research. I would also like to extend my sincere gratitude to my thesis committee members: Prof. K. Mukherjee, Prof. K. N. Subramanian and Prof. T. L. Bieler.

TABLE OF CONTENTS

TABLE OF CONTENTS	iv
LIST OF TABLES	vi
LIST OF FIGURES	viii
CHAPTER I. INTRODUCTION	
1.1 Fabrication of Particulate Reinforced Metal Matrix Composites	1
1.2 Aging Kinetics in Aluminum Alloys.....	10
1.3 Aging Kinetics in MMCs	13
1.4 Interface in MMCs	18
1.4.1 SiC / Aluminum interface	19
1.4.2 Al ₂ O ₃ / Aluminum interface	20
1.5 Fracture of PRMMCs	21
CHAPTER II. MATERIALS AND EXPERIMENTAL PROCEDURES	
2.1 Materials.....	30
2.2 Aging	31
2.3 Metallographic Preparation	31
2.4 Electropolishing and TEM Sample Preparation	32
2.5 Fracture Toughness Testing	33
2.6 Bend Testing	34
CHAPTER III. RESULTS AND DISCUSSION	
3.1 Microstructure Characterization.....	38
3.2 Interface Characterization	42
3.2.1 Al ₂ O ₃ /6061Al interface	42
3.2.2 SiC/6061Al interface.....	46
3.2.3 Observation of moisture effect on interfaces	48
3.3 Aging Kinetics.....	53

3.4 Fracture Behavior	57
3.4.1 Crack initiation.....	57
3.4.2 Crack propagation	62
3.5 Fracture Toughness	72
CHAPTER IV. CONCLUSIONS	
LIST OF REFERENCES	78
APPENDIX	83

LIST OF TABLES

Table 1. Properties of reinforcement (particulate Al_2O_3), a matrix alloy (6061Al), and a composite (15 % Al_2O_3 / 6061Al) [10,12~14].	9
Table 2. Nominal chemical composition (weight percent) 6061 aluminum alloys [17]. .	12
Table 3. Observation of accelerated aging in various MMC systems.	15
Table 4. Properties of matrix alloy (6061Al), and PRMMCs [10,12].	30
Table 5. Descriptions of metallographic preparation for optical and SEM samples.	32
Table 6. Average microhardness values for several PRMMCs during aging. Standard deviation values are in parentheses. (Unit: Hv)	55
Table 7. Data for the effect of aging on fracture mechanisms along the crack path for the PRMMCs.....	67
Table 8. Fracture toughness(K_{Ic}) values for the various PRMMCs as a function of aging conditions. (Unit: $\text{MPa}\sqrt{\text{m}}$, unit of values in parentheses: $\text{Ksi}\sqrt{\text{in}}$)	75

LIST OF FIGURES

Figure 1. Schematic diagram for fabrication of particulate metal matrix composite by vortex method [6].	3
Figure 2. Schematic diagram for fabrication of particulate metal matrix composite by compocasting [5].	5
Figure 3. Fabrication flow chart of PRMMCs by powder metallurgy (PM) [11].	6
Figure 4. Schematic diagram for fabrication of particulate metal matrix composite by spray deposition [5].	8
Figure 5. Illustrative micrograph for crack propagation mechanism at the crack tip in particulate reinforced metal matrix composite (15% (Al ₂ O ₃) _p /2014Al composite), a) reinforcement/matrix interface debonding, b) through particle fracture, c) crack propagates through reinforcement/matrix interface of fractured particle, d) matrix failure, e) fractured particle around the crack, f) crack tip, g) reinforcement/matrix interface debonding ahead of the crack tip, h) fractured particle ahead of the crack tip.	29
Figure 6. Optical micrographs showing various specimens for mechanical testing and typical location of hardness indents, a) hardness indentation placed well between the reinforcement particles, b) half-inch width (B=0.5) short bar fracture toughness specimen, c) half-sectioned and mounted fracture toughness specimen for crack propagation observation, d) double-notched 4-point bend bar specimen for crack initiation observation.	35
Figure 7. A schematic diagram showing the half-inch width short bar fracture toughness specimen [52].	36
Figure 8. A schematic illustration for the dimension of a double notched 4-point bend test specimen. Linear dimensions given are in inches.	37
Figure 9. Three dimensional optical micrographs of PRMMCs showing partial anisotropy and reinforcement clustering along the extruded direction, a) 10% (Al ₂ O ₃) _p /6061Al, b) 20% (Al ₂ O ₃) _p /6061Al, c) 10% SiC _p /6061Al, d) 20% SiC _p /6061Al	39
Figure 10. Distribution in particle size and average particle size (APS) for the composite materials, a) 10% (Al ₂ O ₃) _p /6061Al, b) 20% (Al ₂ O ₃) _p /6061Al, c) 10% SiC _p /6061Al, d) 20% SiC _p /6061Al.	40

Figure 11. Optical micrographs of PRMMCs, a) 10% (Al₂O₃)_p/6061Al, b) 20% (Al₂O₃)_p/6061Al, c) 10% SiC_p/6061Al, d) 20% SiC_p/6061Al. 41

Figure 12. SEM micrographs showing matrix/reinforcement interface region of the (Al₂O₃)_p/6061Al composites, a) irregular interface structure between (Al₂O₃)_p and the matrix alloy indicating a chemical reaction by partial consumption of (Al₂O₃)_p, b) electrochemically extracted reinforcement particles showing MgAl₂O₄ crystals formed on the Al₂O₃ particulates., c) an alumina particulate covered nearly 100% with spinel (MgAl₂O₄) crystals (~ 1 μm), d) individual octahedral-shape MgAl₂O₄ crystals..... 43

Figure 13. TEM micrographs showing the interface of the (Al₂O₃)_p/6061Al composites, a) bright field image of interface region showing formation of MgAl₂O₄ at the Al₂O₃/6061Al interface with irregular interface between the MgAl₂O₄ and the Al₂O₃ particle, b) convergent beam electron diffraction pattern on the MgAl₂O₄ spinel (FCC spinel structure), c) convergent beam electron diffraction pattern on the Al₂O₃ particle (α-Al₂O₃ corundum structure). 45

Figure 14. SEM micrographs showing matrix/reinforcement interface of the SiC_p/6061Al composites, a) arrows indicating formation of interfacial reaction products; dark and short rod-like phase around the SiC particles, b) electrochemically extracted SiC particles, c) an SiC particle showing extensive formation of hexagonal platelets of aluminum carbide (Al₄C₃) growing at the SiC/6061Al interface, d) magnified image showing the hexagonal, Al₄C₃ phases with rejected elemental silicon on its surface..... 47

Figure 15. SEM micrographs showing the moisture sensitivity of the SiC/6061Al interface, a) metallographically prepared SiC_p/6061Al composite showing interfacial reaction products (indicated by arrows) around SiC particles, b) the interfacial reaction products are dissolved (indicated by arrows) by immersing into water for 48 hours showing pits. 49

Figure 16. Observation of moisture effect on the SiC/6061Al and Al₂O₃/6061Al composite interface using ESEM: a) as extracted SiC/6061Al; as electrochemically extracted SiC particle showing sharp edges in the hexagonal shape of Al₄C₃ platelets, b) 65 hours moisture environment of SiC/6061Al; dull edges and cracks in swollen Al₄C₃ platelets indicating dissolution of the interface reaction product, c) 120 hours moisture environment of SiC/6061Al; remarkably dissolved Al₄C₃ platelets showing the hydrophilic property of the interface in 20% SiC_p/6061Al composite. The SiC particle indicated by the arrow, however, remains the same thorough out the moisture absorption, d) as extracted Al₂O₃/6061Al; as electro-chemically extracted Al₂O₃ particle showing formation of MgAl₂O₄ at the interface, e) 65 hours moisture

environment of $\text{Al}_2\text{O}_3/\text{6061Al}$; no change on the interface, f) 120 hours moisture environment of $\text{Al}_2\text{O}_3/\text{6061Al}$; no change on the interface. 50

Figure 17. Magnified images for observation of moisture effect on the $\text{SiC}/\text{6061Al}$ interface using ESEM showing severe dissolution of hexagonal shaped Al_4C_3 platelets, a) as extracted Al_4C_3 particles, b) 20 hours moisture absorption, c) 65 hours moisture absorption, d) 120 hours moisture absorption (all micrographs are at the same magnification) 52

Figure 18. Microhardness variation for several PRMMCs and the complimentary unreinforced matrix alloy as a function of aging time (aging temp. 180°C). Accelerated aging is indicated by the curve peaks shifting to the left..... 54

Figure 19. Observation of crack initiation processes in 20% $(\text{Al}_2\text{O}_3)_p/\text{6061Al}$ composite by conducting 4-point bend testing on double-notched bar specimens, a) before the test (UA), b) after the test (UA) showing extensive plastic deformation around the notch tip (a magnified view(5 \times) of area I is shown in Figure 20), c) before the test (OA), d) after the test (OA), the arrows indicating the void nucleation at the reinforcements and link up by matrix failure..... 58

Figure 20. Magnified images of notch tip area in PRMMCs from post-tested 4-point bend bar specimens, a) magnified image from Figure 19b, arrows indicating fractured particles around the notch tip and tendency for void initiation at sharp edges of the reinforcements, b) magnified image from Figure 21d showing preferential crack propagation path through SiC_p cluster regions and SiC_p clusters link up via matrix failure. 59

Figure 21. Observation of crack initiation processes in 20% $\text{SiC}_p/\text{6061Al}$ composite by conducting 4-point bend testing on double-notched bar specimens, a) before the test (UA), b) after the test (UA) showing preferential crack initiation at the interface of the particles, c) before the test (OA), d) after the test (OA) showing preferential crack propagation through SiC_p cluster regions, and link up of the microcracks by matrix failure (a magnified view(5 \times) of area II is shown in Figure 20)..... 61

Figure 22. SEM images of the actual crack propagation in 20% $(\text{Al}_2\text{O}_3)_p/\text{6061Al}$ composite (UA) and a corresponding illustrative drawings of the crack path profile and damage enclave (indicated by dashed lines) consisting of fractured particles left in the crack wake (note that 'X'= transparticle fracture, and 'O'= interface debonding)..... 63

Figure 23. SEM images of the actual crack propagation in 20% $\text{SiC}_p/\text{6061Al}$ composite (UA) and a corresponding illustrative drawings of the crack path profile and damage enclave (indicated by dashed lines) consisting fractured particles left in the crack wake (note that 'X'= transparticle fracture, and 'O'= interface

debonding), a) 20^v/o (Al₂O₃)_p/6061Al composite (UA), b) 20^v/o SiC_p/6061Al composite (UA). 64

Figure 24. Effect of aging on fracture mechanisms along the crack path for the PRMMC's. 20^v/o (Al₂O₃)_p/6061Al composite shows the transparticle fracture as dominant fracture mechanism irrespective of aging conditions. 20^v/o SiC_p/6061Al composite shows the interface debonding as dominant fracture mode without significant variation due to aging. 66

Figure 25. SEM micrographs showing the crack tip of the PRMMC's, a) crack tip of 20^v/o (Al₂O₃)_p/6061Al composite(OA) showing the extensive particle cracking around the crack tip, b) 20^v/o SiC_p/6061Al composite (PA) showing preferential crack propagation through SiC particulate clustered region and microcrack link up between the particulate clusters. 69

Figure 26. SEM fractography of 20^v/o (Al₂O₃)_p/6061Al composite(OA), a) morphology of fracture surface, b) cracked Al₂O₃ particles, c) both transparticulate fractured and interface debonded Al₂O₃ particle, d) transparticulate fractured Al₂O₃ particle. 70

Figure 27. SEM fractography of 20^v/o SiC_p/6061Al composite(OA), a) morphology of fracture surface, b) interface debonded SiC particles, c) transparticulate fractured SiC particle, d) interface debonded SiC particle. 71

Figure 28. Comparison of fracture toughness (K_q) variation for the PRMMC's as a function of aging time (three specimens were tested to obtain each data point).74

Chapter I

INTRODUCTION

1.1 Fabrication of Particulate Reinforced Metal Matrix Composites

A composite material is defined as a material system composed of two or more constituents, which are essentially insoluble in each other, that form a new material with specific properties usually different from the constituents [1].

Generally, a composite material contains one or more reinforcement phases or constituents for strengthening. The matrix material confines the reinforcements and allows for stress redistribution. Aluminum, magnesium, and titanium are commonly used as matrix materials. Alumina, boron, graphite, and silicon carbide are representatives of ceramic reinforcements used in metal matrix composites (MMCs). All of these reinforcements can be produced as continuous fibers, but silicon carbide and alumina are usually available as discontinuous whiskers. Silicon carbide, boron carbide, alumina, and titanium carbide are often used in the form of a discontinuous particulate. Discontinuous reinforced metal matrix composites (DRMMCs) contain either whiskers or particulates reinforcement or both [2].

Discontinuous whisker and particulate reinforced metal matrix composites have shown superior isotropy and ductility with low fabrication cost, as compare to continuous fiber reinforced metal matrix composites. With the smallest aspect ratio, the particulate reinforced metal matrix composites (PRMMCs) have shown exceptional isotropy for

formation of near-net-shape microstructure and great formability for large volume applications. PRMMCs are also amenable to conventional casting, powder metallurgy processes and metal working. Inexpensive particulate reinforcements such as SiC and Al₂O₃ have been the likely choices for use in PRMMCs. PRMMCs exhibit superior mechanical properties, such as high stiffness-to-weight and strength-to-weight ratio, improved wear resistance and low thermal expansion coefficient, as compared to unreinforced aluminum alloy [2~4].

Fabrication processes for PRMMCs have been developed to produce optimum interfacial strength and uniform particulate distribution with the lowest level of contamination and inclusions. Due to a high surface tension of the molten matrix, efforts have been made on the fabrication of PRMMCs to improve the wettability between ceramic reinforcements and matrix without excessive interfacial reaction. The wettability can be improved by the pre-treatments of reinforcements. such as coating, pre-heating and chemical cleaning. Various fabrication methods of the PRMMCs including ingot metallurgy (IM) (i.e. casting), powder metallurgy (PM) and spray deposition are briefly introduced in the following paragraph [5~11].

Figure 1. shows the vortex method for fabrication of PRMMCs. The reinforcements are mixed and dispersed into the molten matrix by vigorous stirring. The molten alloy is stirred at high speed to create a vortex, while adding reinforcements into the vortex. Optimum wetting can be achieved by continuous stirring after completion of adding reinforcements. This method can utilize the conventional casting apparatus with minimum modification.

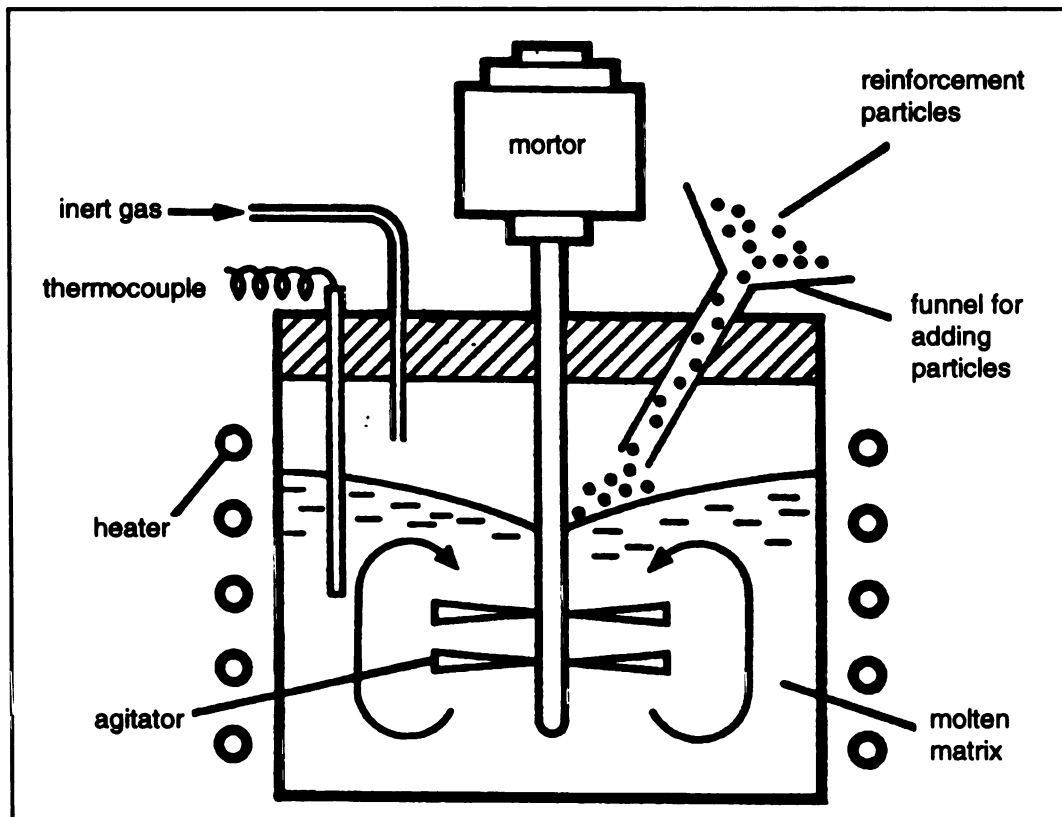


Figure 1. Schematic diagram for fabrication of particulate metal matrix composite by vortex method [6].

However, the large amount and fine size ($< 50 \mu\text{m}$) of reinforcements are difficult to incorporate with the vortex method due to the high surface tension of molten matrix alloy. The recent development by DURALCAN[®] shows a stir casting method without the formation of a vortex, which contains an arrangement of a reactor and a special stirrer under a vacuum environment [5,6].

The schematic drawing of an apparatus for compocasting is shown in Figure 2. The compocasting consist of vigorous stirring of a semi-solid alloy upon casting, while adding the particulate reinforcements to the surface. The ceramic reinforcements are mechanically entrapped into the matrix, which is in between a solidus and liquidus state, even without wetting due to the agitation. The interface bonding can be achieved by abrasive cleaning effect on the particulate reinforcements surface from the continuous stirring throughout the process. Complementary techniques such as gravity casting, injection, squeeze casting, rolling and extrusion can be applied after the compocasting. The compocasting can be advantageous for the fabrication with reinforcements having particularly low wettability and a large aspect ratio. The entrapment of impurities and gases upon agitation can cause the excessive porosities and high level of inclusions. The temperature control for large batch is also a limitation of the compocasting [5,8,9].

The fabrication flow chart of PRMMCs by powder metallurgy (PM) is illustrated in Figure 3. The near-net-shape distribution of fine particulate reinforcements can be achieved by employing the powder metallurgy resulting improvement of ductility and toughness.

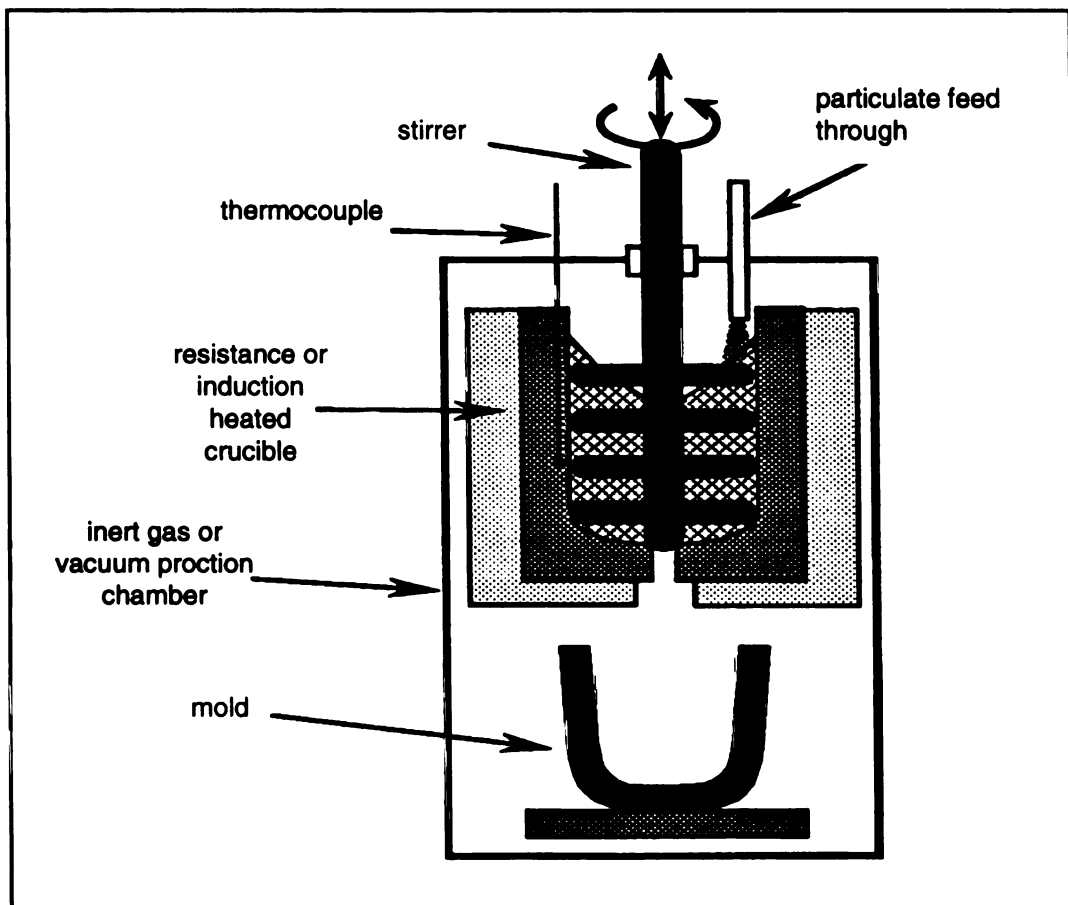


Figure 2. Schematic diagram for fabrication of particulate metal matrix composite by compocasting [5].

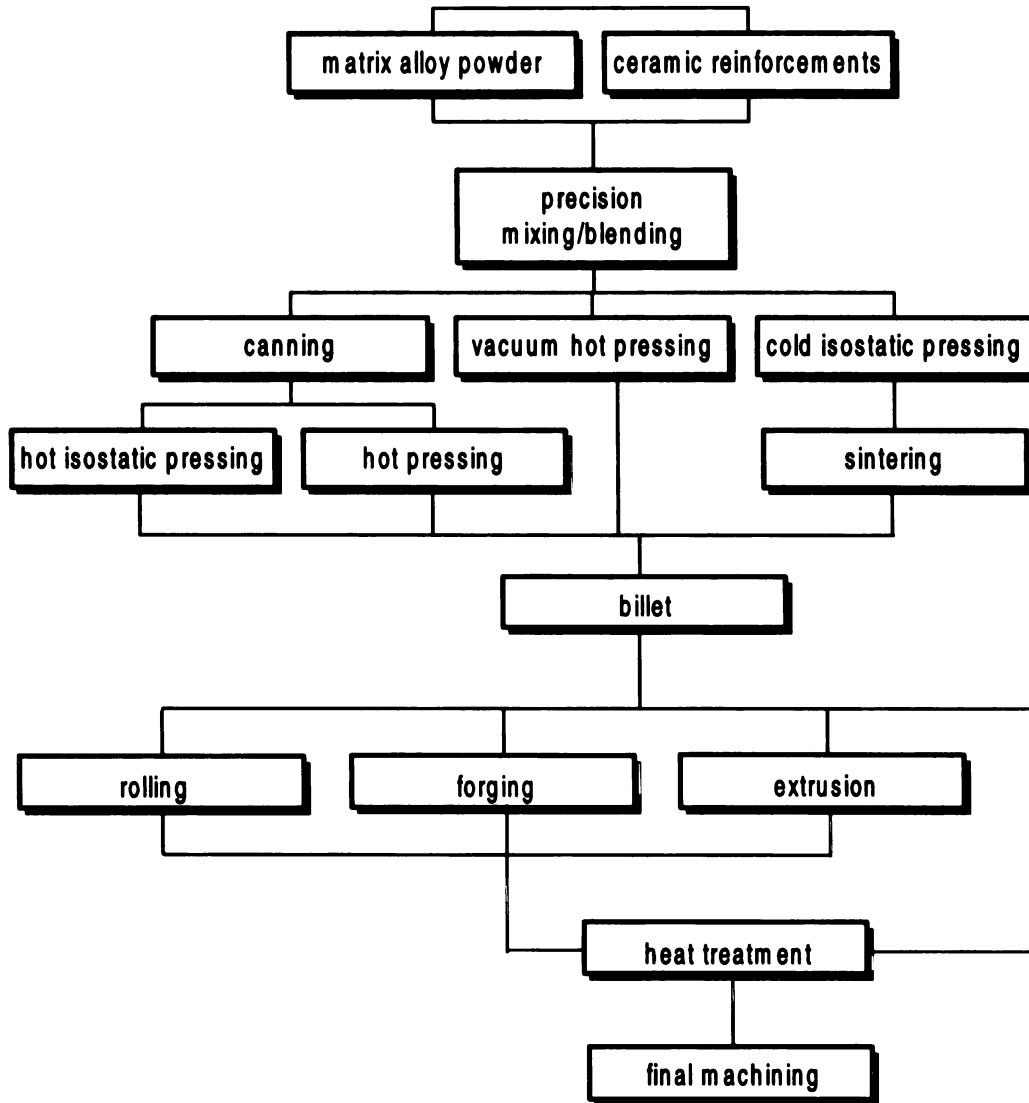


Figure 3. Fabrication flow chart of PRMMCs by powder metallurgy (PM) [11].

The deleterious reaction between reinforcement/matrix interface at high temperature can be avoided by this process, since it is carried out at temperatures below the melting point of the matrix. In spite of producing high quality PRMMCs, the PM is still limited to low volume and high performance applications due to the relatively expensive fabrication costs associated with this method [5,11].

The spray deposition technique for formation of PRMMCs is shown in Figure 4. The fine structures without macro segregation can be achieved by a high speed injection of semi-solidified droplets to the substrate. Due to the rapid solidification rate, the excessive interface reaction can be avoided. The uniform dispersion of particulate reinforcements can be achieved from the dispersion. However, the application of the spray deposition techniques has been limited due to the expensive processing with significantly sensitive deposition parameters, such as substrate temperature, deposition rate, melt superheat, atomizing gas temperature and flow rate [5,10].

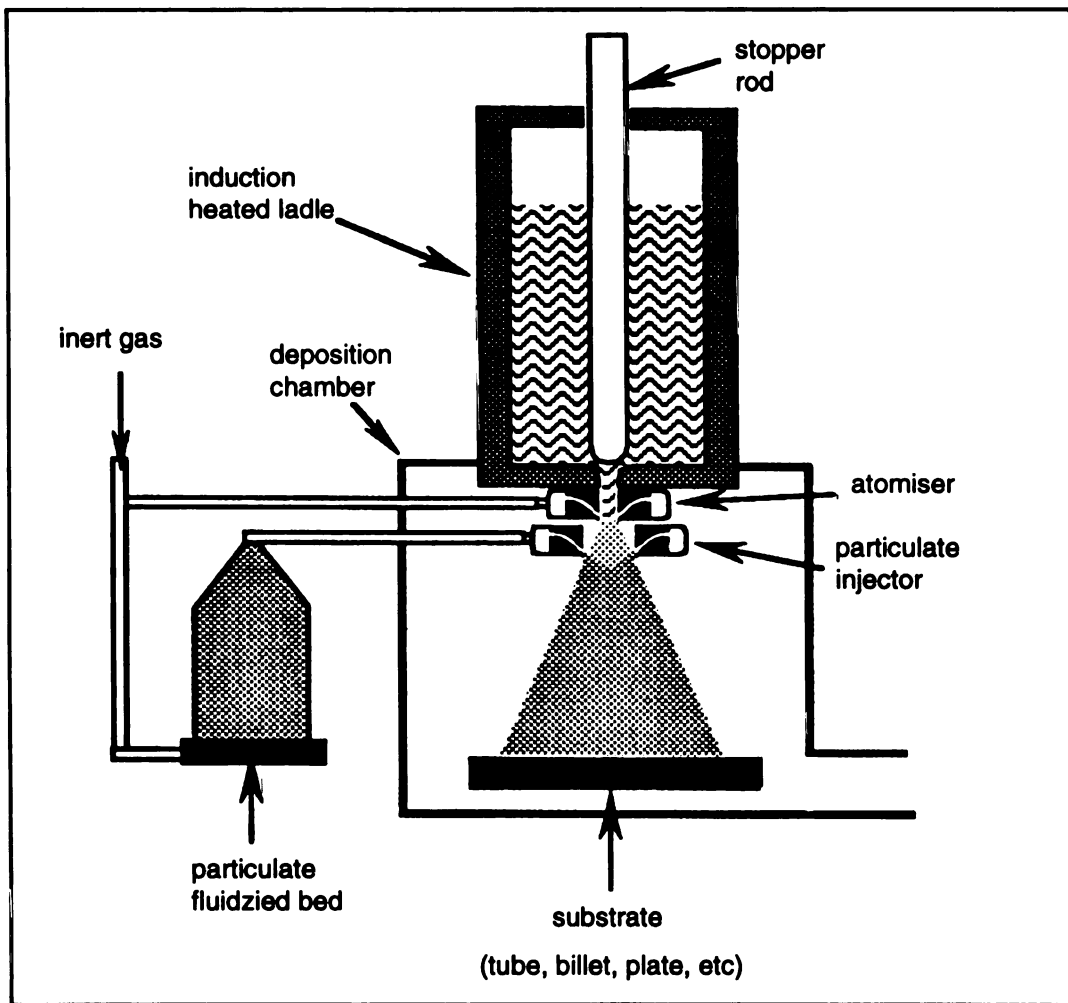


Figure 4. Schematic diagram for fabrication of particulate metal matrix composite by spray deposition [5].

PRMMCs have commanded ample interest due to the potential advantages over monolithic metal alloys in engineering applications. It is known that the addition of ceramic particles into a matrix alloy can generate admirable improvements of mechanical properties, such as specific strength and stiffness, friction, and wear properties. Also, low coefficient of thermal expansion is achievable. Table 1 shows an example of the change of various properties due to the addition of 15% particulate Al_2O_3 into 6061 aluminum alloy. Significant improvements are found in thermal expansion, wear resistance, elastic modulus and ultimate tensile strength with minimal increase in density. Tensile elongation and fracture toughness, however, are considerably reduced by the addition of the particulate reinforcements.

Table 1. Properties of reinforcement (particulate Al_2O_3), a matrix alloy (6061Al), and a composite (15 % Al_2O_3 / 6061Al) [10,12~14].

	Al_2O_3 (particle)	6061 aluminum (T6)	$(\text{Al}_2\text{O}_3)_p$ 15 %/6061Al (T6)
density (g/cm^3)	3.98	2.68	2.86
coefficient of thermal expansion ($10^{-6}/\text{K}$)	7.0	23.4	19.8
*volume loss by wear test (mm^3)	---	8.75	0.0174
elastic modulus (Gpa)	460	69.0	88.9
tensile elongation (%)	---	20	6
ultimate tensile strength (Gpa)	8	0.31	0.37
fracture toughness ($\text{Mpa}\sqrt{m}$)	4	27.0	22.0

*volume loss (mm^3) by block-on-ring wear test (ASTM G-77). 4140 steel (HRC = 50-60) was used for the ring material. Tests performed in 10W40 motor oil for 2 hrs. with a 667-N load at 36 rpm [12].

Engineered variability of mechanical properties is achieved in PRMMCs by the appropriate selection of the type, volume fraction, size, shape of the reinforcement phase and matrix alloy. Such flexibility allows the PRMMCs to meet performance requirements deemed difficult using monolithic materials. Tailored PRMMCs enable the automotive, aerospace and military industry to achieve improved materials performance with traditional fabrication methods at reasonable costs. However, the lack of fracture toughness and tensile ductility are the major limitations of PRMMCs in structural application. Efforts have been made to improve the low ductility and toughness in PRMMCs [15].

1.2 Aging Kinetics in Aluminum Alloys

Strengthening of aluminum alloys by heat treatment can be achieved by the following processes: solution heat treatment for dissolution of soluble phases, quenching for development of supersaturation and age hardening for precipitation of solute atoms. The solution heat treatment sets the maximum practical amount of the soluble hardening elements such as copper, magnesium or silicon into solid solution in the aluminum matrix. Quenching is performed in order to produce a supersaturated solid solution (SSS) which preserves the solid solution state formed during solution heat treating at temperatures of 450~550°C. Dislocations are generated from the quenching of the solution heat treated aluminum alloys due to quenching strains, condensation of excess vacancies and differential contraction in constituents or dispersoid particles. Age hardening is achieved from either natural aging at room temperature (about –20°C to 60°C) or artificial aging at a moderately elevated temperature (less than about 250°C).

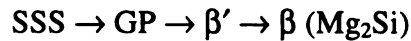
During natural aging and at initial periods of artificial aging, redistribution of the solute elements in the supersaturated solid solution (SSS) occurs forming clusters or GP (Guinier-Preston) zones with lattice structure coherency. These precipitates nucleate preferentially at heterogeneous sites such as grain boundaries, dislocations, and dispersoid particles having greater disorder and higher energy. The GP zones generally form a disk, a needle, or a sphere like shape, and are located parallel to some low-index plane of the matrix lattice, in the size range of $10 \sim 100 \text{ \AA}$ in diameter. The alloying elements determine the shape, orientation, and size of the GP zones. The formation of GP zone produces coherency strain by the distortion of lattice planes. The distorted region provides additional interference to dislocations when they move to cut through the GP zones. The strengthening effect is caused by the additional stress required to move a dislocation through the GP zones. The maximum strength of the alloy results from a high density of fine GP zones or precipitates interacting with dense dislocations. The GP zones are characteristically metastable. Hence, the GP zones are converted or dissolved into equilibrium precipitates which become incoherent with crystal structure of the parent lattice, as aging temperature or time is increased. This transition of precipitates occurs when the strength of the interfacial bond is exceeded by growth of the GP zones accompanying increase in coherency strains. The transition to equilibrium precipitates increases interparticle spacing and results in dislocations to loop around rather than to cut through the precipitates. The effect of strengthening accordingly decreases with the growth of the equilibrium precipitates. Hence, the following three mechanisms are associated with precipitation hardening. The first is 'strain hardening' in which the strain fields impede the dislocation motion and result in an increase of flow stress. The strain

fields are caused from the nucleation of the coherent particles with slightly different lattice parameters. The second is 'chemical hardening' which is caused by an increased number of solute-solvent bonds from the presence of the solution-rich zones. The additional stress is required for dislocation motion. The last mechanism is 'dispersion hardening' in which the dislocation motion is blocked by obstacles from the dispersion of fine precipitates [16].

Table 2. Nominal chemical composition (weight percent) 6061 aluminum alloys [17].

Al	Cu	Mg	Si	Mn	Cr	Zn	Fe	Ti	Others
balance	0.15 ~	0.8 ~	0.4 ~	0.15	0.04 ~	0.25	0.7	0.15	0.15
	0.4	1.2	0.8	max.	0.35	max.	max.	max.	max.

The composition range of 6061 aluminum alloy (Al-Mg-Si) is in Table 2 and, the precipitation sequence for the alloy may be described as follows:



The first stage of precipitation tends to occur in the $\langle 001 \rangle$ direction from the supersaturated solid solution with a fine needle-like shape. These GP zones are about 60 Å in diameter and 200 to 1000 Å in length with a minor coherency strain. However, others contended that GP zones are initially spherical in shape and eventually evolve into needle-like shapes [18]. With an increase in aging time, GP zones are transformed into β' transition precipitates which have a three dimensional rod-like shape with a highly ordered Mg_2Si structure. The detailed sequence of precipitation consists of SSS,

vacancy-silicon clusters, vacancy rich coherent Al-Mg-Si GP zones, partially coherent and disordered needle-shape phase in $\langle 100 \rangle$, partially coherent and ordered needle-shape phase aligned in $\langle 100 \rangle$ directions, semicoherent hexagonal rod-shape phase, and equilibrium Mg_2Si platelets. Hardening of the alloy system results from the additional hindrance to dislocation motion by the stress required to break magnesium-silicon bonds in the zones and transition precipitates [19].

1.3 Aging Kinetics in MMCs

The nucleation and growth kinetics of precipitation in an aluminum alloy can be significantly changed by the addition of a ceramic reinforcement to the matrix. Consequently, such change in the aging kinetics of the matrix can alter the overall properties of MMCs. Numerous investigations have clearly verified that age hardening behavior of the MMCs, which are fabricated by either powder metallurgy (PM) or ingot metallurgy (IM), is quite different from that of the unreinforced matrix [20~36]. The accelerated aging has been extensively observed in discontinuously (i.e. whisker or particulate) reinforced MMCs as compared to the unreinforced matrix alloy.

Results of earlier study on 23% $\text{SiC}_w/\text{6061Al}$ MMC (PM) [20] showed that accelerated aging was primarily due to the high dislocation density generated from the thermal expansion mismatch between the reinforcement and the matrix, and due to the presence of a highly diffusive interface in the MMC. Consequently, both factors increased the diffusivity of precipitate-forming elements, and thus change the aging kinetics influencing solute/vacancy diffusion.

Dislocation generation due to the thermal expansion mismatch was observed by *in-situ* High Voltage Electron Microscope (HVEM) study on 20% SiC_w/6061Al (PM) composite. In this work, the generation of dislocations at Al/SiC interface and subsequent nucleation of precipitates on the dislocations were clearly observed upon cooling from the annealing temperature [21,22].

An investigation of 13.2 % SiC_w/2124Al MMC (PM) [23] revealed an increase in dislocation density due to SiC_w reinforcements. Transmission electron microscope (TEM) showed dislocations punched out from the whisker end upon cooling. The increased dislocation density caused by thermal expansion mismatch provided the heterogeneous nucleation sites for strengthening precipitation with resultant accelerated aging [23].

Another investigation [24], employing differential scanning calorimetry (DSC), also found that the precipitation and dissolution kinetics were accelerated in SiC reinforced MMCs, such as 8 and 20% SiC_w/2124Al (PM), 20% SiC_w/2219Al (PM) and 20% SiC_p/6061Al (PM). However, the overall age hardening sequence of the MMCs was not changed by the addition of SiC reinforcements, as compared to their unreinforced matrix alloys. Effect of solution heat treatment on 6061 Al alloy is minimum as compared to other aluminum alloys. Hence, the monolithic 6061Al alloy is known as quench-insensitive alloy [16]. In addition, the quench-insensitive 6061 aluminum alloy was observed to become quench-sensitive by the addition of SiC_p, which promoted the precipitation of GP zones or the intermediate phase during quenching [24].

Two principal mechanisms regarding accelerated aging have emerged from the theoretical and experimental studies of 10% SiC_w/6061Al (PM) composite [25]. One is a

dislocation dominant mechanism involving large-sized reinforcement phase (whisker radii $>1\ \mu\text{m}$) and high dislocation density ($>10^{14}\ \text{m}^{-2}$) which states that the dislocations serve as heterogeneous nucleation sites for precipitation. The other is a residual stress dominant mechanism involving small-sized reinforcement phase (whisker radii $< 0.25\ \mu\text{m}$) and low dislocation density ($<10^{13}\ \text{m}^{-2}$) which suggests that residual stress induces the diffusion of solute atoms [25].

Accelerated aging is consistently observed in various MMC systems. Some are listed in table 3.

Table 3. Observation of accelerated aging in various MMC systems.

Reinforcement / Matrix	Processing Method	Particle Size	Reference
30 ^v % SiC/7091Al	powder metallurgy	$\sim 5\ \mu\text{m}$	[27]
20 ^w % SiC _p /8090Al	powder metallurgy	$\sim 3\ \mu\text{m}$	[28]
17 ^v % SiC _p /2014Al	powder metallurgy	---	[29]
13.9 ^v % SiC _p /6061Al	powder metallurgy	---	[30]
15 ^v % (Al ₂ O ₃) _p /6061Al	powder metallurgy	---	[31]
10 & 15 ^v % (Al ₂ O ₃) _p /6061Al	ingot metallurgy	$0.5 \sim 25\ \mu\text{m}$	[32]

The size and shape of the reinforcement control the intensity of dislocation generation and resultant aging kinetics. It was reported that the intensity of dislocation generation was lowest for small, nearly spherical particles ($< 1\ \mu\text{m}$), but increased with increasing

particle size (1~5 μm). The sharp corner of particulates or whisker ends also showed intense generation of dislocations due to an increased local strain [21,22].

The interfacial reactions in MMCs can influence the aging kinetics by changing the chemical composition of the matrix. The rejection of silicon was found from the interface reaction by remelting 10% $\text{SiC}_p/6061\text{Al}$ (IM) composite. A hardness increase was observed by the presence of the additional silicon in solid solutions [33]. On the other hand, migration of matrix magnesium to the interface was found in the 10% $(\text{Al}_2\text{O}_3)_p/6061\text{Al}$ (IM) composite. During the solidification, magnesium in the matrix diffused to the interface to form a reaction product MgAl_2O_4 resulting in possible change in matrix aging kinetics [34].

At the constant volume fraction, the average dislocation density was decreased by increase of reinforcement size, hence, accelerated aging was considerably less in MMCs with relatively large reinforcements [21,22,26]. Consequently, mechanical properties such as hardness and strength were improved in a MMC with a small particle or whisker size (~5 μm) which has higher dislocation density or a smaller mean free path between heterogeneous nucleation sites [35].

The difference of aging kinetics was reported between powder metallurgy (PM), such as cold packed vacuum sintering, and ingot metallurgy (IM), such as stir casting. Even though the kinetics of aging in ingot metallurgy (IM) processed materials are remarkably slower than those observed in powder metallurgy (PM) processed materials [24], accelerated aging was observed for the MMCs fabricated by both the PM and the IM process [20~32].

Furthermore, the type and amount of precipitation in the matrix were also affected by the amount of reinforcement. It was found that the addition of 15% $(\text{Al}_2\text{O}_3)_p$ to 6061Al increased the dislocation density slightly more than that of 10% $(\text{Al}_2\text{O}_3)_p$. Consequently, microhardness for as-quenched matrix was elevated with the addition of alumina particles. The increased strength of these materials apparently resulted from the high dislocation density in the composite matrix [32].

Solution treatment temperature also affects aging kinetics in MMCs. The effect of solution heat temperature was observed by using two different temperatures (529°C and 557°C) on 13.9% SiC_p /6061Al (PM) MMC [30]. The increase in hardness was more pronounced for composite with solution heat treated at 557°C, as compared to its monolithic 6061 aluminum. Therefore, greater dislocation density in the matrix was achieved from the higher solution heat treatment temperature under solidus temperature upon quenching.

The influence of an aging temperature was also examined on 17% SiC_p /2014Al (PM) MMC employing various aging temperatures from 150°C to 195°C. Accelerated aging increased with aging temperature over the range of 150°C to 195°C. Upon aging at the highest temperature (195°C), the maximum accelerated aging was accomplished by the heterogeneous nucleation of fast growing S' precipitation (CuAlMg_2) on the dense dislocations. As the aging temperature was decreased, heterogeneous nucleation of GP zones, with low growth rate, became dominant over S' formation. Clearly, the extent of accelerated aging in matrix depends on the aging temperature [29].

Accelerated aging is associated with the coefficient of thermal expansion mismatch (ΔCTE) between the matrix and the reinforcement with a result of an increased dislocation density and/or enhanced diffusion. The strain fields generated by ΔCTE , upon quenching, are relaxed by the formation of dislocations in the matrix. The increased dislocations due to the ΔCTE can serve as sites for the heterogeneous nucleation of strengthening precipitates and as a short circuit of the diffusion path for solute atoms [36]. Furthermore, the elastic fields from residual stress around the reinforcements can induce the enhanced diffusivity at relatively low dislocation density and/or large particle size [25].

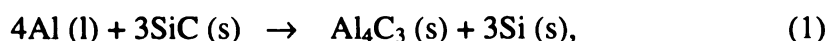
1.4 Interface in MMCs

The nature of the interface in metal matrix composites is the most important for tailoring mechanical properties since the maximum mechanical strength of MMCs is achieved by the proper load transfer from the matrix to the reinforcement. The efficiency of the load transfer strongly depends on the bonding strength of the interface and the optimum bonding strength can be attained from the formation of adequate reaction layer at the interface. Eventually, the interface reaction can improve the wettability of ceramic/metal system from the development of interfacial phases on the interface. However, the poor adhesion of the interface can result from the formation of brittle intermetallic compound due to a massive reaction. Interface debonding, upon loading, can be caused by poor adhesion resulting in strength decrease of MMCs. Hence, the interface reaction may have either beneficial results, by increasing the ductility and the fracture toughness, or deleterious effects, by causing crack initiation points. The interface

reaction is controlled by the matrix composition, the type of reinforcement, the fabrication method and the heat treatment [35~48].

1.4.1 SiC / Aluminum interface

Intermetallic compounds form at a SiC/aluminum interface [37~42]. A typical reaction is given as follows:



where the (l) and (s) represent liquid and solid respectively. The reaction product, Al_4C_3 , is a brittle and hydrophilic compound which is detrimental to mechanical properties of MMCs. Excessive formation of Al_4C_3 at interface of a composite may result in overall degradation of mechanical properties, such as reduction of reinforcement and interfacial strength and an increase in corrosion sensitivity. [38,39]. The change of matrix composition was also observed in that the hardness of the matrix was increased due to the additional silicon rejection from the interface reaction [33]. The formation of Al_4C_3 is mainly due to the prolonged contact between SiC and molten aluminum [37,40,42].

From the interface investigation on compocasted $\text{SiC}_p/6061\text{Al}$ MMC [40], with as-received and oxidized SiC_p , no reaction products were found at the as-received SiC_p interface. During this time, the MgAl_2O_4 was formed at the interface of oxidized SiC_p by the reaction between SiO_2 layer and molten aluminum. However, a significant amount of Al_4C_3 was found at the interface between as-received SiC_p and the matrix by remelting the composite at 800 °C for 20 min. Thus, the formation of Al_4C_3 depends on the casting route. Compocasting, which has a reduced fabrication time at a high temperature (above 650°C), can prevent the formation of the interfacial product.

The morphology of the SiC/aluminum interface was recently revealed by the observation of electrochemically extracted SiC particles from a spray formed 20% SiC_p/2024Al composite. Massive reaction products formed during a 24-hour heat treatment at 560°C and 640°C. Elevated growth rate was noted at higher temperature, 640°C. SEM examinations showed that SiC particles were covered with Al₄C₃ platelets, having a HCP crystal structure. Dendrites of elemental Si were also present. Si exhibits a diamond cubic structure. It was found that the Al₄C₃ was formed at moderately elevated temperature, ~450°C [41].

The extent of formation of Al₄C₃ at the interface can be altered by controlled processes; such as an addition of silicon to the matrix alloy to prevent the interfacial reaction by increased free silicon in the matrix [42], a suitable fabrication route without prolonged contact between SiC particles and molten aluminum [38,40,43], and formation or coating of some oxide layer like SiO₂ and TiO₂ on the SiC reinforcement [44].

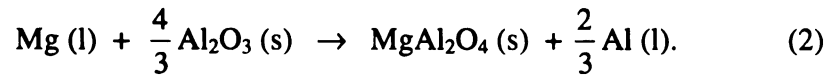
1.4.2 Al₂O₃ / Aluminum interface

Wettability and bonding at the Al₂O₃/aluminum interface are improved by the formation of spinels (MgAl₂O₄) from the interface reaction. Spinel promotes strengthening of the interface by forming strong bonds with metals and ceramics [34,45~47]. The interface product, MgAl₂O₄, forms when sufficient contact occurs over time between alumina and molten aluminum alloy [45].

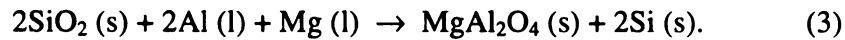
Pertaining to interface in Al₂O₃ short fiber (Saffil) and Al-Mg (2~3%) alloy composite, magnesium diffusion toward interface was observed upon solidification and heat treatment at 500°C. Magnesium diffused and reacted with the alumina fibers and

silica coatings forming interfacial reaction products, such as MgO, MgAl₂Si, Mg₂Si and Si. Magnesium diffuses continuously to the interface during heat treatment where it in turn reacts to produce Si and Mg₂Si precipitation in the matrix [47].

A detailed interface characterization of 10% (Al₂O₃)_p/6061Al (IM) composite revealed the following. The morphology of MgAl₂O₄ single crystal was revealed by electrochemical dissolution of the conductive matrix alloy around the alumina particles. The alumina particles were almost fully covered with MgAl₂O₄ (spinel) of average size 1 µm. MgAl₂O₄ single crystals were grown at the surface of the alumina particle by the following chemical reaction:



The reaction occurs between molten aluminum and solid alumina particles when segregation of magnesium at the interface region results. Another possible reaction between SiO₂ and molten matrix was also considered as the following reaction:



However, the reaction between SiO₂ and molten matrix was suggested to be less significant in this observation [34].

1.5 Fracture of PRMMCs

It is generally known that the embedded ceramic particles in a matrix alloy, which forms a composite material, usually generate admirable improvements of mechanical and physical properties, such as high specific strength and stiffness, enhanced friction and

wear capabilities, and low coefficient of thermal expansion. However, tensile elongation and fracture toughness of PRMMCs are reduced considerably by the addition of the particulate reinforcements. Compared to the matrix alloy, the lack of the fracture toughness and tensile ductility limits the use of particulate reinforced metal matrix composites (MMCs) in structural applications in spite of other advantageous properties. Even though PRMMCs show significantly lower fracture toughness and tensile ductility, fracture still occurs by a ductile rupture mechanism similar to that of matrix material. The failure process of unreinforced alloys and MMCs alike arises by a sequence of void nucleation, growth and coalescence [3,4].

In PRMMCs, void nucleation tends to occur by the following processes; (i) by transparticle cracking and/or (ii) by particle/matrix interface debonding [49~53]. The crack propagates by the matrix failure resulting from link-up of microfracture defects and coalescence of microvoids. Void nucleation is strongly influenced by the composite material's microstructural composition including particulate shape, size and volume fraction, and matrix temper by aging [52,54~61]. The interfacial bonding strength between reinforcement and matrix critically affects void nucleation of the PRMMCs. The formation of brittle intermetallic compounds and other phases at the reinforcement/matrix interface, such as Al_4C_3 , can cause premature void nucleation at the interface resulting in decreased load transfer efficiency [38,39]. Reinforcement content (V_f) and matrix heat treatment also influence void nucleation, and consequently, the resultant mechanical properties of MMCs. Fracture toughness usually decreases with an increase of reinforcement volume fraction. Also, studies show that unlike the matrix alloy, neither

the fracture toughness nor tensile elongation recover upon over aging of the MMCs [50,53,56,59].

Void nucleation in particulate reinforced metal matrix composites were studied using acoustic emission monitoring during tensile testing [57]. Three volume fractions (5, 10 and 20 %) and three sizes (nominally 3, 10, 30 μm) of SiC_p reinforced in 1070Al and 5050Al were investigated to observe the effects of microstructural parameters on the fracture behavior. It was observed that the void nucleation occurred from the onset of plastic deformation and continued throughout the plastic regime. Both particle cracking and interface debonding were observed as a mode of the void nucleation. The rate of damage initiation increased with particle size and volume fraction. However, the damage initiation was independent from the matrix composition and heat treatment. It was concluded that the failure strain or ductility of the composites was not controlled solely by void nucleation at the reinforcements, but local failure processes occurring in the matrix during void growth and coalescence [57].

The fracture toughness of discontinuous reinforced metal matrix composites (DRMMCs) with different reinforcement type, particulate size and matrix alloy was observed for $\text{SiC}/\text{A356Al}$, $\text{B}_4\text{C}/\text{A356Al}$, $\text{SiC}/\text{A201Al}$ and $\text{B}_4\text{C}/\text{A201Al}$ [52]. At a constant reinforcement volume fraction, the fracture toughness increased with an increase in particle size and interparticulate spacing. The fracture toughness of the $\text{B}_4\text{C}/\text{A356Al}$ composite was shown to be substantially lower compared to the $\text{SiC}/\text{A356Al}$ composite. Apparently, the lower fracture toughness in B_4C reinforced MMCs was due to the extensive reaction at the reinforcement/matrix interface and as a consequence matrix

microstructure change due to redistribution of alloying elements during the molten-state of the composite processing. Discontinuous crack growth for fracture of DRMMCs was also suggested from employing the acoustic emission and metallographic technique. The discontinuous crack growth process occurred by a rather strict sequence of failure: the initial transparticular fracture or reinforcement/matrix interface debonding and following ductile failure in the interparticular ligaments by void coalescence.

The effect of particle size was studied with the ~50 % $\text{SiC}_p/\text{Mg}(4\text{w}\%)$ -Al (IM) composite with a particle size of 3.5 ~ 165 μm . The particle size effect is suggested to be exclusively related to the incidence of damage in the composite. In four point flexural tests, particle cracking was shown to occur in the larger particles when the probability of the cracking increased as the particle size increased. Particle cracking reduces the flow strength of the materials and subsequent crack coalescence controlled the ultimate strength and ductility [58].

The effect of particle size on fracture toughness was also studied on 20% $\text{SiC}_p/1100\text{Al}$ with 2.4, 3.2, 8 and 20 μm average particle size. Fracture toughness, K_{Ic} , was not improved with the increase of particle size in this particular study [61]. Hence, the K_{Ic} fracture toughness was independent of the SiC particulate size up to 20 μm average size. For constant particle size, the K_{Ic} fracture toughness was indicated to be decreased with increased volume fraction that retained smaller interparticle space. The fracture toughness was not changed with an increase of the particle size at the same volume fraction. The K_{Ic} fracture toughness was mainly dependent on the volume

fraction of SiC particles [61]. Other studies, however, have reported an increase in fracture toughness with increasing particle size [26, 52]

The effect of aging conditions on fracture properties were studied with the 15 & 20% SiC_p/Al-Zn-Mg-Cu (PM) composite. Unlike an unreinforced matrix alloy, significant differences in fracture initiation and growth toughness were observed due to aging conditions. Both fracture initiation and growth toughness of materials in the UA condition were about two times higher than that of in the OA condition. The toughness decrease between materials in the UA and the OA conditions was due to the transition in the local fracture mode from SiC particle cracking to the SiC_p/matrix near interface debonding. Void nucleation by particle cracking impedes void coalescence by a constraining matrix flow, leading to a increase in ductility and fracture toughness. The SiC_p volume fraction affected the fracture initiation toughness which decreased linearly with an increase in the volume fraction of SiC_p [53].

From a study of tensile behavior on 20% SiC_p/6061Al (IM) composite, the T4 tempered composite showed more particle cracking than the T6 tempered composite throughout the gauge length. More particle cracking in the T4 condition was due to extensive plastic strain distribution in the gage length of the composite. In contrast, localized strain was found for material in the T6 condition so that the fracture was initiated in the clusters of reinforcement particles. Fracture in a reinforcement clustering zone was a result of, not only particle cracking, but also fracture of the matrix ligaments with high triaxial stress due to the elastic misfit and the plastic constraint of the particles. Crack initiation and growth were due to the fracture of the matrix in the clustering zone

together with any fracture of the particles in the zone. Subsequently, cracks linked by fast fracture through the matrix to adjacent clustering zones, resulting in macroscopic fracture [50].

Fracture behavior of 20% SiC_p/7XXXAl (PM) composite was studied focusing on microstructural variables, such as the SiC particle size and matrix temper. A strong effect of aging was correlated to an increased fracture occurring by particle/matrix interface debonding in OA condition. The dominant mode of the fracture at UA condition was particle cracking with preferential fracture of large particles. The increase of interface debonding on OA condition was due to the precipitation at the SiC particle/matrix interface which reduced the interfacial bond strength. The reduced interfacial strength caused by the precipitation may affect the lack of recovery in fracture toughness in OA condition. By conducting 4-point bend test on double notched bar composite specimens, preferential crack initiation was observed in clustered particle regions. Consequently, particle clustering plays a major role in determining the strength-fracture relationship in PRMMCs regardless of matrix temper [59].

The influence of aging condition on the fracture toughness was studied on 15% (Al₂O₃)_p/2014Al (IM) and 15% (Al₂O₃)_p/6061Al (IM) [56]. The fracture toughness of the MMCs decreased with aging from UA to OA condition, and no recovery of fracture toughness was found in OA condition, unlike the unreinforced matrix alloy. The lack of recovery of fracture toughness in OA condition was due to the strain localization caused by the formation of ligaments upon the fracture of the reinforcement particles. The ligaments showed earlier fracture in OA condition by the formation of secondary

microvoids within the ligaments which were due to the presence of large second-phase precipitates in the matrix. Remarkably, no reinforcement/matrix interface failure was found at any aging condition in these MMCs.

A comparison of fracture properties between particulate reinforced (SiC_p) and whisker reinforced (SiC_w) MMCs is observed from the investigation on $\text{SiC}_p/6061\text{Al}$ and $\text{SiC}_w/6061\text{Al}$ composites. The $\text{SiC}_p/6061\text{Al}$ MMC exhibited moderately superior strength, ductility, fracture toughness and crack propagation resistance, as compared to the $\text{SiC}_w/6061\text{Al}$ composite [60].

Crack propagation was observed by *in-situ* deformation of 15% $(\text{Al}_2\text{O}_3)_p/6061\text{Al}$ (IM). The *in-situ* observation was conducted on tensile specimens by scanning electron microscope (SEM) focused on the crack tip region. Microcracks were observed both near and ahead of the crack tip region. Microcracking ahead of the crack occurred in a region which was considerably larger than the inter-particle spacing. Crack propagation mechanisms were sequential processes involving initiation of microcracks, link-up of microcracks with macrocrack by matrix failure, and growth of macrocracks [54].

Void nucleation occurs at the reinforcements in PRMMCs. The mode of void nucleation has been observed by two dominant ways: through particle cracking and particle/matrix interface debonding [49~54]. Figure 5 shows the illustration for the fracture mechanism around the tip of a crack, such as reinforcement/matrix interface debonding, through particle fracture, and matrix failure. Figure 5 also shows the void nucleation in the plastic deformation zone nearby the crack. The crack propagates by the matrix failure which result from link-up, growth and coalescence of microvoids. The

mode of void nucleation is intensely influenced by microstructural parameters in PRMMCs [38,39,50,53,56,57]. The reinforcement size and the bonding strength of a reinforcement/matrix interface are the significant parameters controlling void nucleation of the PRMMCs. The increase of particle size causes a change from interface debonding to particle cracking resulting in an increase in fracture toughness [58]. The formation of brittle intermetallic compound at reinforcement/matrix interface can cause the void nucleation at the interface, resulting in a decrease in load transfer efficiency [38,39]. The volume fraction of reinforcement and matrix heat treatment are also important parameters for void nucleation. Fracture toughness is observed to be decreased with an increase of a reinforcement volume fraction and is not recovered at OA condition, unlike the unreinforced matrix alloy [50,53,56]. The increase of particle size and volume fraction of the reinforcement causes an increase in void nucleation rate. However, the void nucleation rate is independent of matrix heat treatment which controls the yield strength and ductility of PRMMCs. The ductility of PRMMCs, hence, is not influenced by void nucleation but by matrix failure processes, such as void growth and coalescence [57]

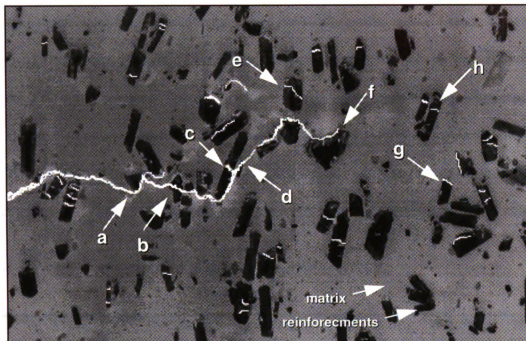


Figure 5. Illustrative micrograph for crack propagation mechanism at the crack tip in particulate reinforced metal matrix composite (15% $(\text{Al}_2\text{O}_3)/2014\text{Al}$ composite), a) reinforcement/matrix interface debonding, b) through particle fracture, c) crack propagates through reinforcement/matrix interface of fractured particle, d) matrix failure, e) fractured particle around the crack, f) crack tip, g) reinforcement/matrix interface debonding ahead of the crack tip, h) fractured particle ahead of the crack tip.

Chapter II

MATERIALS AND EXPERIMENTAL PROCEDURES

2.1 Materials

The materials investigated were the 6061 aluminum alloy based PRMMCs, $(\text{Al}_2\text{O}_3)_p/6061\text{Al}$ and $\text{SiC}_p/6061\text{Al}$. Both composites consisted of 10 and 20 volume percent (%) reinforcement. The composite materials were fabricated by Duralcan Inc., San Diego, CA, using a stir-melt cast process, and received as extruded bars, 19 mm thick and 77 mm wide. Unreinforced commercial 6061 aluminum alloy was also investigated for comparison. Typical mechanical values of as-received material are given in Table 4.

Table 4. Properties of matrix alloy (6061Al), and PRMMCs [10,12].

	6061Al (T6)	10 % $(\text{Al}_2\text{O}_3)_p$ /6061Al(T6)	20 % $(\text{Al}_2\text{O}_3)_p$ /6061Al(T6)	10 % SiC_p /6061Al(T 6)	20 % SiC_p /6061Al(T6)
elastic modulus (GPa)	69.0	81.4	97.2	--	103.4
tensile elongation (%)	20	10	4	--	5.5
ultimate tensile strength (MPa)	276	296	352	--	496.4
fracture toughness ($\text{MPa}\sqrt{m}$)	29.7	24.1	21.5	24.7	20.5

2.2 Aging

All specimens were solution heat treated at 550°C for 90 minutes and quenched in ice brine. Artificial aging was conducted at 180°C, immediately after the solution heat treatment to prevent the natural aging at room temperature. Aging was accomplished over a 12-step time sequence ranging from 1 to 3,000 minutes.

Hardness testing was conducted using a Leco[®] M-400-G microhardness tester equipped with a Vickers diamond pyramid indenter. A 10 gram load was used to obtain the change in hardness due to aging. Hardness indentations were taken exclusively in matrix regions avoiding contact between the indenter and the reinforcement phase. At least 10 hardness readings were taken for each composite sample. Figure 6a shows that indentation is placed well between the reinforcement particles indicating no contact between the indenter and the reinforcement phase.

2.3 Metallographic Preparation

Metallographic preparation for PRMMCs is significantly different in comparison to the preparation of monolithic alloys. Polishing of PRMMCs is more difficult due to the large hardness difference between the metal matrix and the ceramic reinforcement. The extruded composite bars were sectioned into cubes (10 mm × 10 mm × 10 mm) for the heat treating using a silicon carbide impregnated abrasive wheel cutter and a precision diamond saw. After the aging, the composite specimens were encapsulated in a metallographic mount, 1¼ inch (3.175 mm) in diameter, for polishing. Initial grinding of the polishing process was accomplished using an 120 grit zirconia/alumina abrasive belt polisher. The mounted specimens were subsequently polished on a lapping wheel using

30 μm , 6 μm and 1 μm diamond suspensions. The final polishing step was conducted using 0.06 μm colloidal silica suspension on a vibratory polisher (Buehler Vibromet II®) for 2 hours. Detailed description of this procedure is given in Table 5.

Table 5. Descriptions of metallographic preparation for optical and SEM samples.

step 1	Section as extruded 19 mm thick and 77 mm wide bars into 10×10×10(mm) cubes using a silicon carbide impregnated abrasive wheel cutter and a precision diamond saw.
step 2	Heat treatments (Solution heat treatment and artificial aging).
step 3	Metallographic mount in 1¼ inch diameter by thermoplastic Lucite.
step 4	Remove major roughness using zirconia/alumina impregnated abrasive belt polisher (120 grit.).
step 6	8 inch lapping wheel polisher for 3 steps, 30 μm diamond suspension with *ULTRA-PAD® cloth, 6 μm diamond suspension with *POLIMET® cloth, and 1 μm diamond suspension with *TEXMET 2000® cloth. Each step is taken for ~5 minutes.
step 7	Final polishing (~2 hours) by vibratory polishing machine *VIBROMET 2® using *MASTERMET® (0.06 μm colloidal silica suspension) with *TEXMET 2000® cloth.

*Products from BUEHLER® Inc.

2.4 Electropolishing and TEM Sample Preparation

In order to obtain more details of the interface morphology, the aluminum matrix was removed by electro-chemical dissolution with a potential of 10 DC volts and 22 Amp current in 5°C electrolyte composed of 33% HNO_3 /67% methanol solution. The $(\text{Al}_2\text{O}_3)_p$ /6061Al composites were electro-chemically dissolved for 5 minutes and cleaned with methanol. Care was taken to limit the exposure of SiC_p /6061Al composites to a

moist environment due to the hydrophilic nature of the interfacial reaction products (Al_4C_3). Electrochemical dissolution for the $\text{SiC}_p/6061\text{Al}$ composites was allowed for ~3 minutes and followed by cleaning in acetone immediately. The reinforcement phase was extracted from the matrix by electrochemical dissolution. The extracted particles were observed with a Hitachi S-2500C[®] scanning electron microscope (SEM). The observation of moisture effect on the interface of $\text{SiC}_p/6061\text{Al}$ composite was observed by immersing of electro-chemically extracted SiC particles into de-ionized water in the Electroscan 2020[®] environmental scanning electron microscope (ESEM).

Specimens for transmission electron microscope (TEM) examination were prepared from peak aged (PA) 20% $(\text{Al}_2\text{O}_3)_p/6061\text{Al}$ and 20% $\text{SiC}_p/6061\text{Al}$ composites to characterize the interface microstructure. Mechanically-thinned (~100 μm) composite specimens were electropolished by a Dimpler[®] machine until about 20 μm thickness was achieved. Final thinning was performed using an argon ion mill at an accelerating voltage of 6 KV with 15 ~ 5° sample inclination to the ion beam. Thin foils were cleaned for 3 minutes with the sample inclination of 20° after a hole was obtained in the foils. TEM examinations were conducted using Philips CM30[®] operated at an acceleration voltage of 200 KV. Convergent beam electron diffraction (CBED) was also performed on the interface regions using a 50 nm electron-beam spot size.

2.5 Fracture Toughness Testing

Fracture toughness tests were conducted on the materials using Fractometer II[®] test system. Half-inch width ($B = 0.5$ in) short bar (SB) specimens were tested according to ASTM 1309 test procedures. A schematic diagram for the chevron notch short bar specimen is given in Figure 7. When conducting a chevron notch SB fracture,

precracking is not necessary since a sharp crack initiates at the apex of the chevron notch ligament in the specimens. A sharp crack at the notch tip can be initiated at relatively low loads due to the high stress concentration. The fracture toughness is determined from the peak load value which occurs when the propagation of crack attains a critical length in the SB specimens [52]. A short bar fracture toughness specimen is shown in Figure 6b. Fracture toughness testing was conducted on specimens in the under aged (UA), peak aged (PA) and over aged (OA) conditions to ascertain the aging effects. Using the SEM, the fracture morphology was assessed by examining fracture surface of PRMMC specimens. The crack propagation path was observed from half-sectioned (transverse to the chevron notch direction) and polished SB specimens using optical and scanning electron microscope. Figure 6c shows a transverse sectioned SB specimen used for the observation of the crack propagation profile.

2.6 Bend Testing

Crack initiation mechanisms were observed using 4-point bend test specimens. A double-notched bar specimen is shown in Figure 6d. The dimension of the bend specimen is also given in Figure 8. In 4-point bend testing, one notch will fail by catastrophic crack growth, while the companion notch will be preserved in a pre-crack propagation deformation state. Crack initiation behavior was observed for 20% $(\text{Al}_2\text{O}_3)_p/6061\text{Al}$ and 20% $\text{SiC}_p/6061\text{Al}$ composites in the UA, PA and OA conditions. Optical micrographs were taken before and after bend tests were conducted on polished surface around the notch tip region to assess changes in crack initiation due to aging effects.

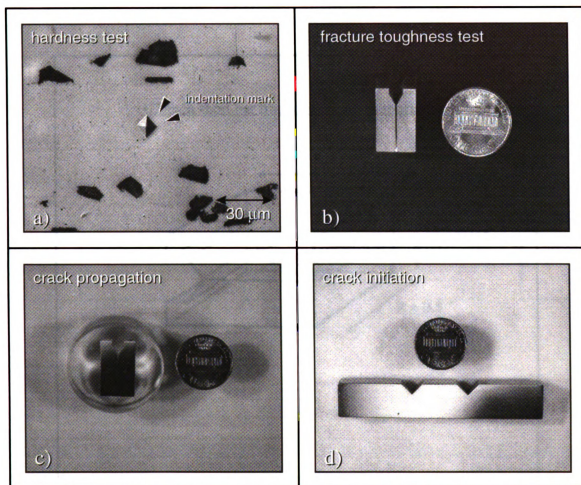


Figure 6. Optical micrographs showing various specimens for mechanical testing and typical location of hardness indents, a) hardness indentation placed well between the reinforcement particles, b) half-inch width ($B=0.5$) short bar fracture toughness specimen, c) half-sectioned and mounted fracture toughness specimen for crack propagation observation, d) double-notched 4-point bend bar specimen for crack initiation observation.

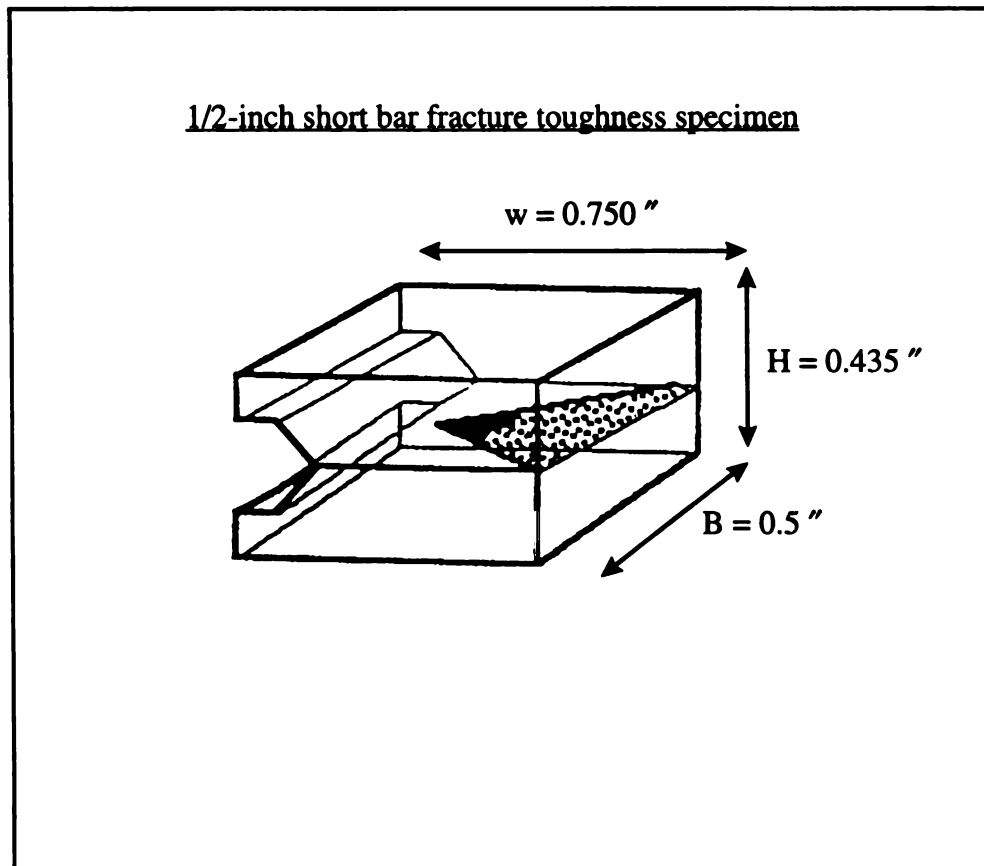


Figure 7. A schematic diagram showing the half-inch width short bar fracture toughness specimen [52].

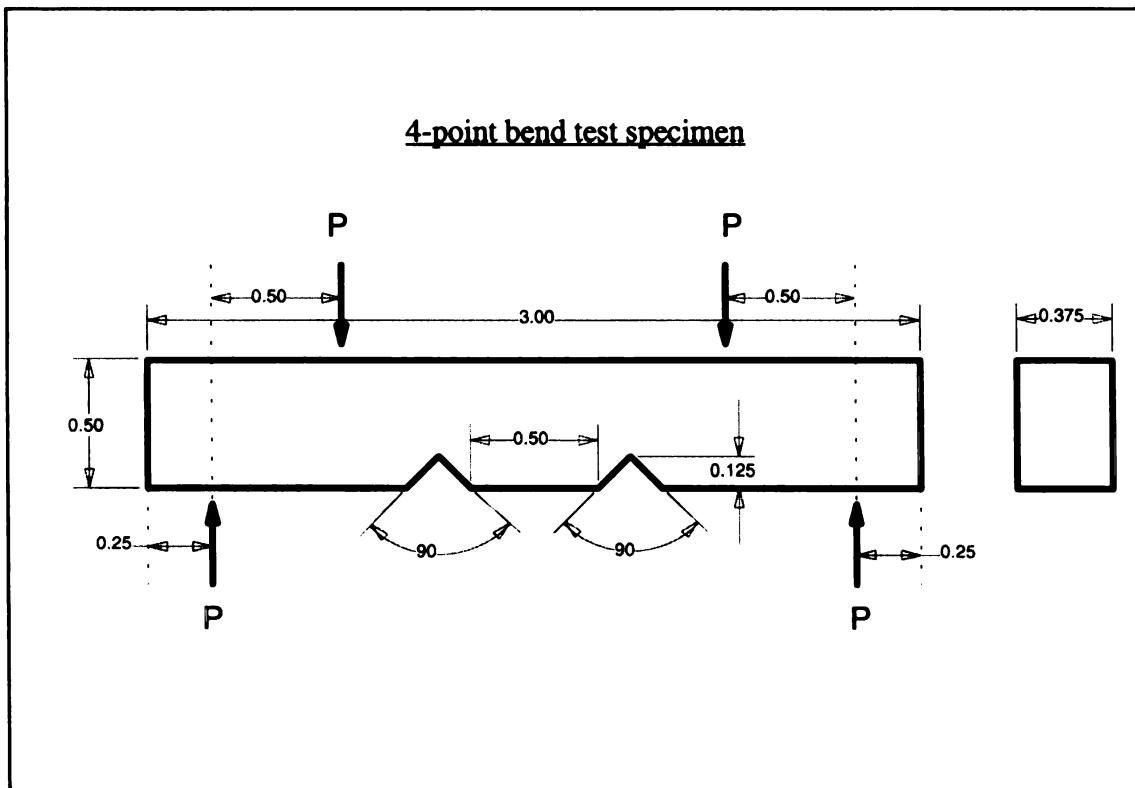


Figure 8. A schematic illustration for the dimension of a double notched 4-point bend test specimen. Linear dimensions given are in inches.

Chapter III

RESULTS AND DISCUSSION

3.1 Microstructure Characterization

Three dimensional optical micrographs of the composite materials used in this study are shown in Figure 9. Microstructural anisotropy and reinforcement clustering are noted, partially, along the extrusion direction. The 10% SiC_p composite shows the smallest particle size distribution with an average particulate size of ~5 μm, while 20% (Al₂O₃)_p reinforced MMC reveals the largest particle size distribution with the average particulate size of ~18 μm. The 10% (Al₂O₃)_p composite shows the average particulate size ~ 9 μm and 20% SiC_p reinforced composite shows the average particulate size ~13 μm. The distribution in particle size is shown in Figure 10 for the composite materials investigated. Interfacial reaction products (appeared small dots) can be seen around the reinforcements in (Al₂O₃)_p composites (Figure 11a and 11b). Regarding the shape, SiC_p tended to be more angular with sharp corners compared to (Al₂O₃)_p. Also, the frequency of particulate clustering in SiC_p reinforced composites appeared to be somewhat greater along with extensive reaction at the particle/matrix interface (Figure 11c and 11d).

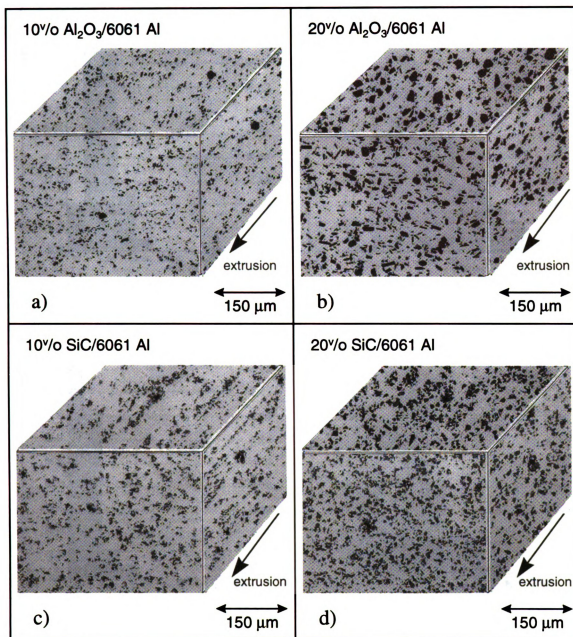
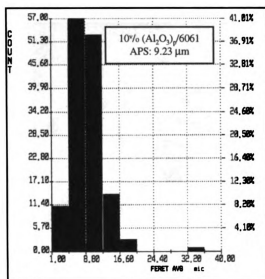
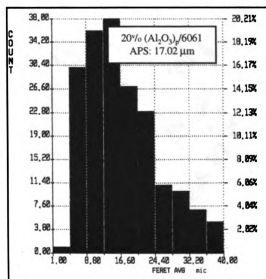


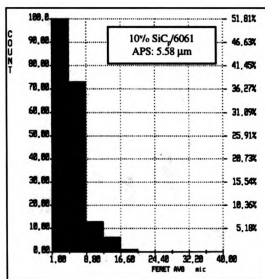
Figure 9. Three dimensional optical micrographs of PRMMCs showing partial anisotropy and reinforcement clustering along the extruded direction, a) 10% $(\text{Al}_2\text{O}_3)_p$ /6061Al, b) 20% $(\text{Al}_2\text{O}_3)_p$ /6061Al, c) 10% SiC_p /6061Al, d) 20% SiC_p /6061Al



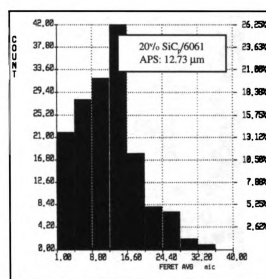
(a)



(b)



(c)



(d)

Figure 10. Distribution in particle size and average particle size (APS) for the composite materials, a) 10% (Al₂O₃)_p/6061Al, b) 20% (Al₂O₃)_p/6061Al, c) 10% SiC_p/6061Al, d) 20% SiC_p/6061Al.

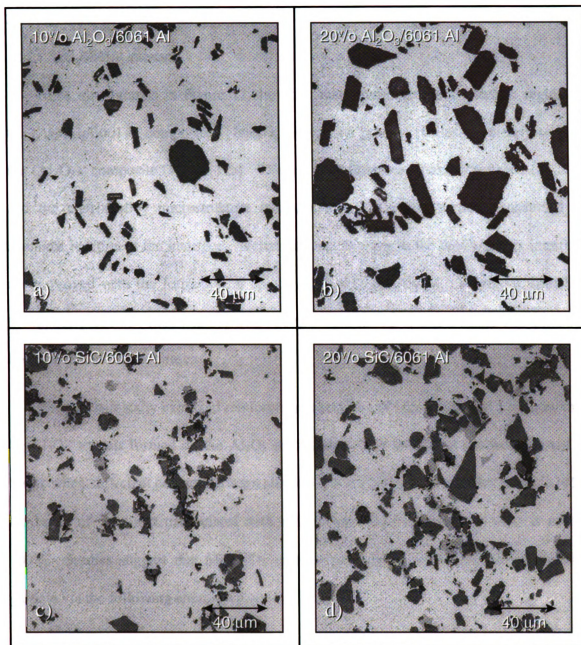


Figure 11. Optical micrographs of PRMMCs, a) 10% (Al₂O₃)_p/6061Al, b) 20% (Al₂O₃)_p/6061Al, c) 10% SiC_p/6061Al, d) 20% SiC_p/6061Al.

3.2 Interface Characterization

3.2.1 Al₂O₃/6061Al interface

SEM micrographs in Figure 12 show the matrix/reinforcement interface region of the (Al₂O₃)_p/6061Al composites. Interfacial reaction product phases are clearly seen in the (Al₂O₃)_p composite (Figure 12a). The irregular interface structure between (Al₂O₃)_p and the matrix alloy microstructure indicates that Al₂O₃ was partially consumed in chemical reaction at the interface. Wettability and bonding at the Al₂O₃/matrix interface are improved with the formation of spinel (MgAl₂O₄) [34,45,47]. Therefore, spinel is thought to promote interfacial bonding strength by forming strong metallic and covalent bonds with the matrix phase.

Electrochemically extracted reinforcement particles in Figure 12b and 12c show that MgAl₂O₄ crystals formed on the Al₂O₃ particulates. The interfacial product, MgAl₂O₄, forms when sufficient contact between alumina and molten aluminum alloy prevails [45]. Coverage of alumina particulates with spinel (MgAl₂O₄) crystals (~ 1 μm) is nearly 100%. Studies suggest that MgAl₂O₄ single crystals grow on the surface of alumina particle via the following chemical reaction [34,46]:

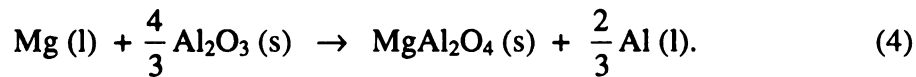


Figure 12d shows the individual octahedral-shape MgAl₂O₄ crystals. Also note that the surrounding areas near individual spinel crystals are preferentially etched. Such regions around the spinel crystals resulted from the rejection of elemental Al during the interfacial reaction according to Equation 4 [34,46].

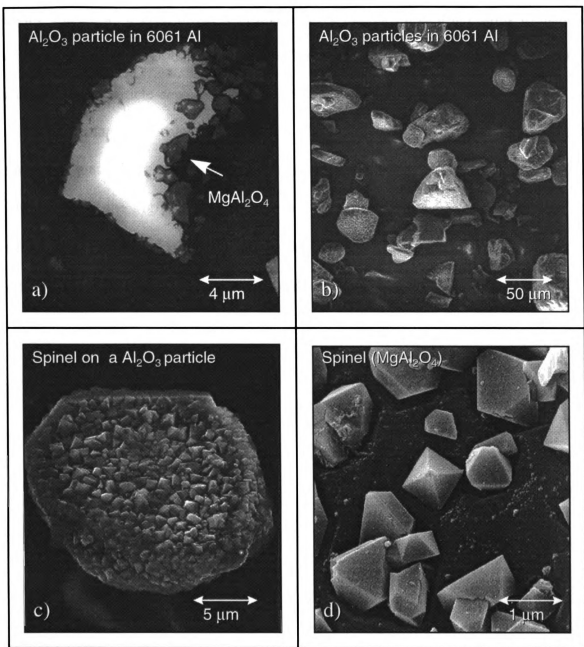


Figure 12. SEM micrographs showing matrix/reinforcement interface region of the $(\text{Al}_2\text{O}_3)_p/6061\text{Al}$ composites, a) irregular interface structure between $(\text{Al}_2\text{O}_3)_p$ and the matrix alloy indicating a chemical reaction by partial consumption of $(\text{Al}_2\text{O}_3)_p$, b) electrochemically extracted reinforcement particles showing MgAl_2O_4 crystals formed on the Al_2O_3 particulates, c) an alumina particulate covered nearly 100% with spinel (MgAl_2O_4) crystals ($\sim 1\ \mu\text{m}$), d) individual octahedral-shape MgAl_2O_4 crystals.

Figure 13a shows a TEM bright field image of the interface region indicating formation of MgAl_2O_4 at the Al_2O_3 /6061Al interface. The irregular interface between the MgAl_2O_4 and the Al_2O_3 particle depicted in the TEM image suggests partial consumption of the Al_2O_3 particulate as revealed earlier (Figure 12a and 12c). Figure 13b and 13c represent the convergent beam electron diffraction patterns (CBED) of MgAl_2O_4 spinel and Al_2O_3 . The CBED of the MgAl_2O_4 corresponds to the $[001]$ zone diffraction pattern of FCC, MgAl_2O_4 spinel. The CBED of Al_2O_3 particulates also corresponds to the $[\bar{4}1\bar{1}]$ zone diffraction pattern of $\alpha\text{-Al}_2\text{O}_3$ with corundum structure.

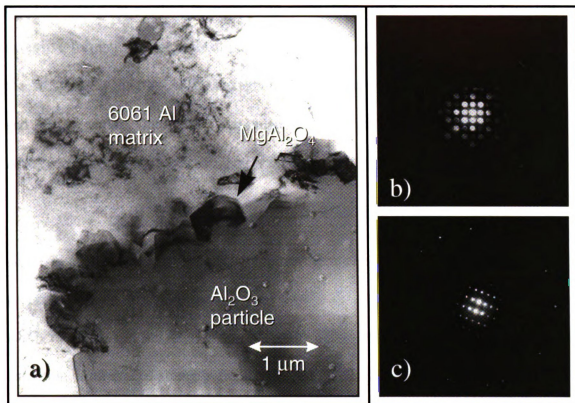
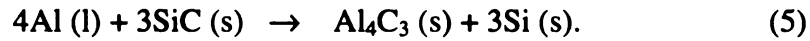


Figure 13. TEM micrographs showing the interface of the $(\text{Al}_2\text{O}_3)_p/6061\text{Al}$ composites, a) bright field image of interface region showing formation of MgAl_2O_4 at the $\text{Al}_2\text{O}_3/6061\text{Al}$ interface with irregular interface between the MgAl_2O_4 and the Al_2O_3 particle, b) convergent beam electron diffraction pattern on the MgAl_2O_4 spinel (FCC spinel structure), c) convergent beam electron diffraction pattern on the Al_2O_3 particle (α - Al_2O_3 corundum structure).

3.2.2 SiC/6061Al interface

SEM micrographs in Figure 14 show the matrix/reinforcement interface of SiC_p/6061Al composites. The arrows in Figure 14a indicate the formation of interfacial reaction products. The black phase and short rod-like phase (arrows in Figure 14a point to these phases) around the SiC particles are typically observed. The morphology of the interfacial reaction product is revealed in more detail in Figure 14b and 14c showing extensive formation of hexagonal platelets of aluminum carbide (Al₄C₃), which grew at the SiC/6061Al interface. The hexagonal Al₄C₃ platelets are on average ~0.7 μm thick and ~3 μm wide. Due to SiC particulate consumption during the interfacial reaction, Al₄C₃ forms as result of the following reaction [37~42,52]:



Al₄C₃ is a brittle and hydrophilic compound that can adversely affect the mechanical properties of metal matrix composites [37~42,52]. Extensive formation of interfacial Al₄C₃ may result in the degradation of mechanical and physical properties, such as the reduction in interfacial strength, fracture strain (ε_f), fracture toughness, and an increase in corrosion sensitivity [38,39]. Previous investigations show that Al₄C₃ forms mainly due to prolonged contact between SiC and molten aluminum alloy [35,37,40,42], however, Al₄C₃ growth is observed also at moderately elevated temperature, ~450°C [41]. Figure 14d represents a the magnified image of the hexagonal, Al₄C₃ phases with some second phase particles attached to its surface. The second phase particles residing on the Al₄C₃ surface is rejected elemental silicon [41] which is typical interfacial reaction in accordance with Equation 5.

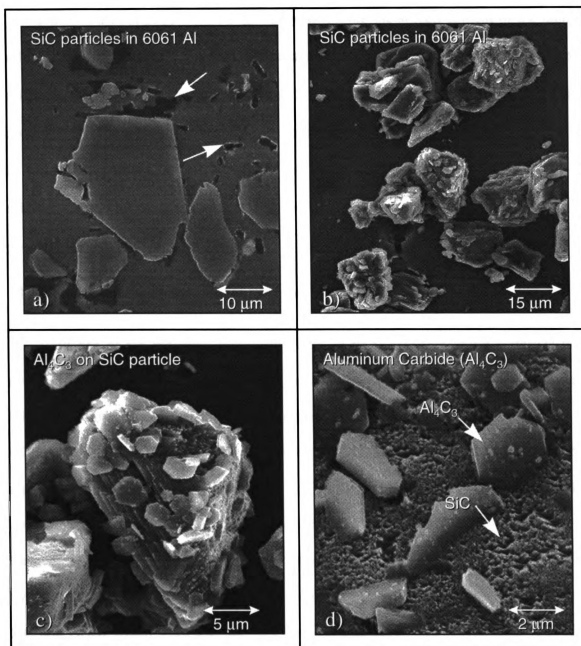
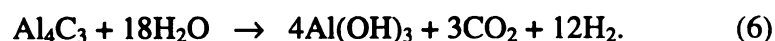


Figure 14. SEM micrographs showing matrix/reinforcement interface of the SiC/6061Al composites, a) arrows indicating formation of interfacial reaction products; dark and short rod-like phase around the SiC particles, b) electrochemically extracted SiC particles, c) an SiC particle showing extensive formation of hexagonal platelets of aluminum carbide (Al_4C_3) growing at the SiC/6061Al interface, d) magnified image showing the hexagonal, Al_4C_3 phases with rejected elemental silicon on its surface.

Formation of Al_4C_3 can be mitigated by increasing the silicon content of the matrix alloy. Addition of Si to the matrix alloy make the forward reaction of Equation 5 more difficult because rejected excess elemental Si will be increased beyond its equilibrium content [42]. Other means of reducing the formation of Al_4C_3 consist of limiting the time in which SiC particulates and molten Al are in contact [38,40,43]. Also, coating SiC reinforcement with oxides, such as SiO_2 and/or TiO_2 will block Al_4C_3 nucleation and growth [44].

3.2.3 Observation of moisture effect on interfaces

Evidence of the moisture sensitivity of SiC/6061Al interface phase materials was revealed further by the etching away of interfacial and near-interface phase materials following immersion of metallographically-prepared specimens into de-ionized water of 48 hours (Figure 15). Figure 15a represents the unexposed specimen and Figure 15b represents the specimen exposed to water for 48 hours. Clearly, Figure 15b shows the dissolution of interfacial products near a cluster of SiC particulates as the pits have formed. Using the ESEM, a more detailed assessment of the moisture effects was made by regarding the change in the interface phase morphology of extracted particulates of SiC and Al_2O_3 which were exposed to a water environment over several time intervals. The ESEM images taken over an elapsed time period of 120 hours show conclusive evidence of dissolution of the Al_4C_3 phase (see Figure 16a,b,c). In contrast, there was virtually no evidence of moisture induced degradation of the spinel phase (MgAl_2O_4) which surrounds aluminum oxide particulate (see Figure 16d,e,f). Dissolution of aluminum carbide in water is given as:



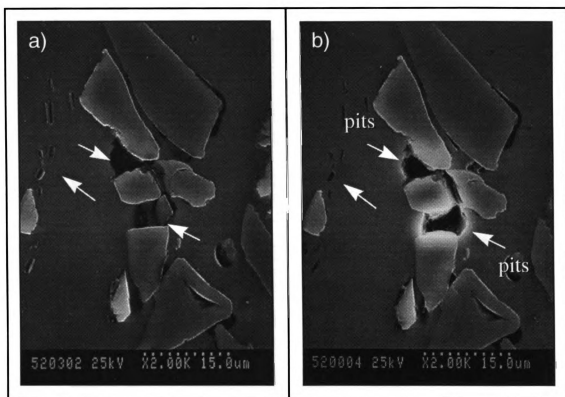


Figure 15. SEM micrographs showing the moisture sensitivity of the SiC/6061Al interface, a) metallographically prepared SiC_p/6061Al composite showing interfacial reaction products (indicated by arrows) around SiC particles, b) the interfacial reaction products are dissolved (indicated by arrows) by immersing into water for 48 hours showing pits.

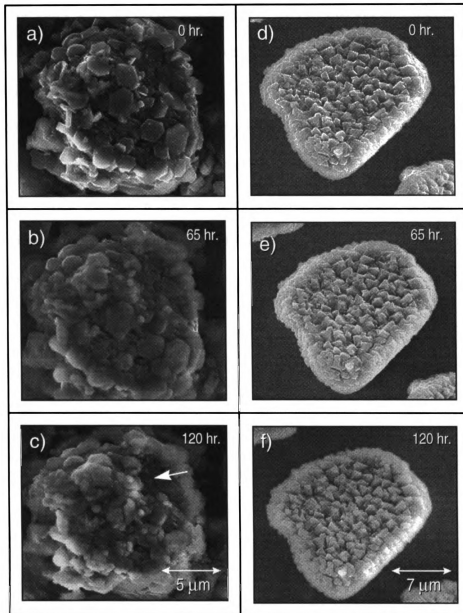


Figure 16. Observation of moisture effect on the SiC/6061Al and Al_2O_3 /6061Al composite interface using ESEM: a) as extracted SiC/6061Al; as electro-chemically extracted SiC particle showing sharp edges in the hexagonal shape of Al_4C_3 platelets, b) 65 hours moisture environment of SiC/6061Al; dull edges and cracks in swollen Al_4C_3 platelets indicating dissolution of the interface reaction product, c) 120 hours moisture environment of SiC/6061Al; remarkably dissolved Al_4C_3 platelets showing the hydrophilic property of the interface in 20% SiC_p/6061Al composite. The SiC particle indicated by the arrow, however, remains the same thorough out the moisture absorption, d) as extracted Al_2O_3 /6061Al; as electro-chemically extracted Al_2O_3 particle showing formation of $MgAl_2O_4$ at the interface, e) 65 hours moisture environment of Al_2O_3 /6061Al; no change on the interface, f) 120 hours moisture environment of Al_2O_3 /6061Al; no change on the interface.

Although the gases were not chemically analyzed, the fact that gas bubbles emerged from the polished surface of a SiC/6061Al composite material when immersed in water enhances the plausibility of the reaction given in Equation 6. It is interesting to note that within 120 hours of exposure to water nearly all the faceted Al_4C_3 crystals were severely degraded by dissolution (see Figure 17). As found in this work, when water is in direct contact with Al_4C_3 , dissolution is quite rapid. It should be noted, however, that the rate of Al_4C_3 dissolution is mitigated somewhat for SiC_p/6061Al composite itself because the exposed surface area of Al_4C_3 is less.

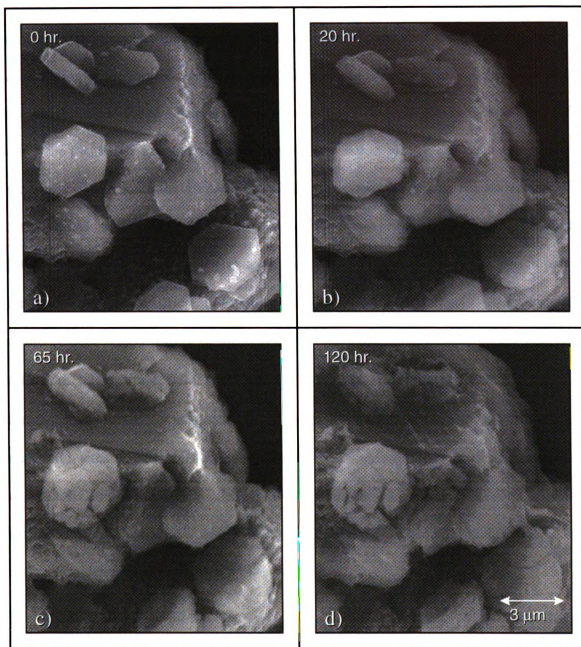


Figure 17. Magnified images for observation of moisture effect on the SiC/6061Al interface using ESEM showing severe dissolution of hexagonal shaped Al_4C_3 platelets, a) as extracted Al_4C_3 particles, b) 20 hours moisture absorption, c) 65 hours moisture absorption, d) 120 hours moisture absorption (all micrographs are at the same magnification) .

3.3 Aging Kinetics

Figure 18 and Table 6 show average microhardness variation for several PRMMCs and the complementary unreinforced matrix alloy as a function of aging time (a complete compilation of the microhardness data table is given in the appendix). Accelerated aging (corresponding to the reduced incubation time to reach the peak hardness) is observed for all of the PRMMCs as relative to the unreinforced matrix alloy. The peak aging time is reduced by ~1.5 hour for 10% (Al₂O₃)_p/6061Al composite and by ~6 hours for 20% SiC_p/6061Al composite. Accelerated aging has been widely observed in PRMMCs [20,24~29,32], and, there is general agreement that the accelerated aging is due in part to the mismatch in the coefficient of thermal expansion (Δ CTE) between the matrix and the reinforcement which results in an increase in the dislocation density and/or enhanced diffusion. The strain field generated by Δ CTE upon quenching is relaxed by the formation of matrix dislocations. Δ CTE induced dislocations serve as heterogeneous nucleation sites for strengthening precipitates. Short circuit of diffusion paths for solute atoms are also enhanced [21]. Additionally, the elastic strain fields from residual stress around the reinforcements can induce the enhanced diffusivity at relatively low dislocation density and/or large particle size [25].

Composites with higher volume fraction of reinforcement (V_f) show higher microhardness values for the solutionized and the as-quenched condition as well. Higher strength results in composites with increasing V_f because of the enhancement in dislocation density from reinforcement/matrix thermal expansion mismatch [32].

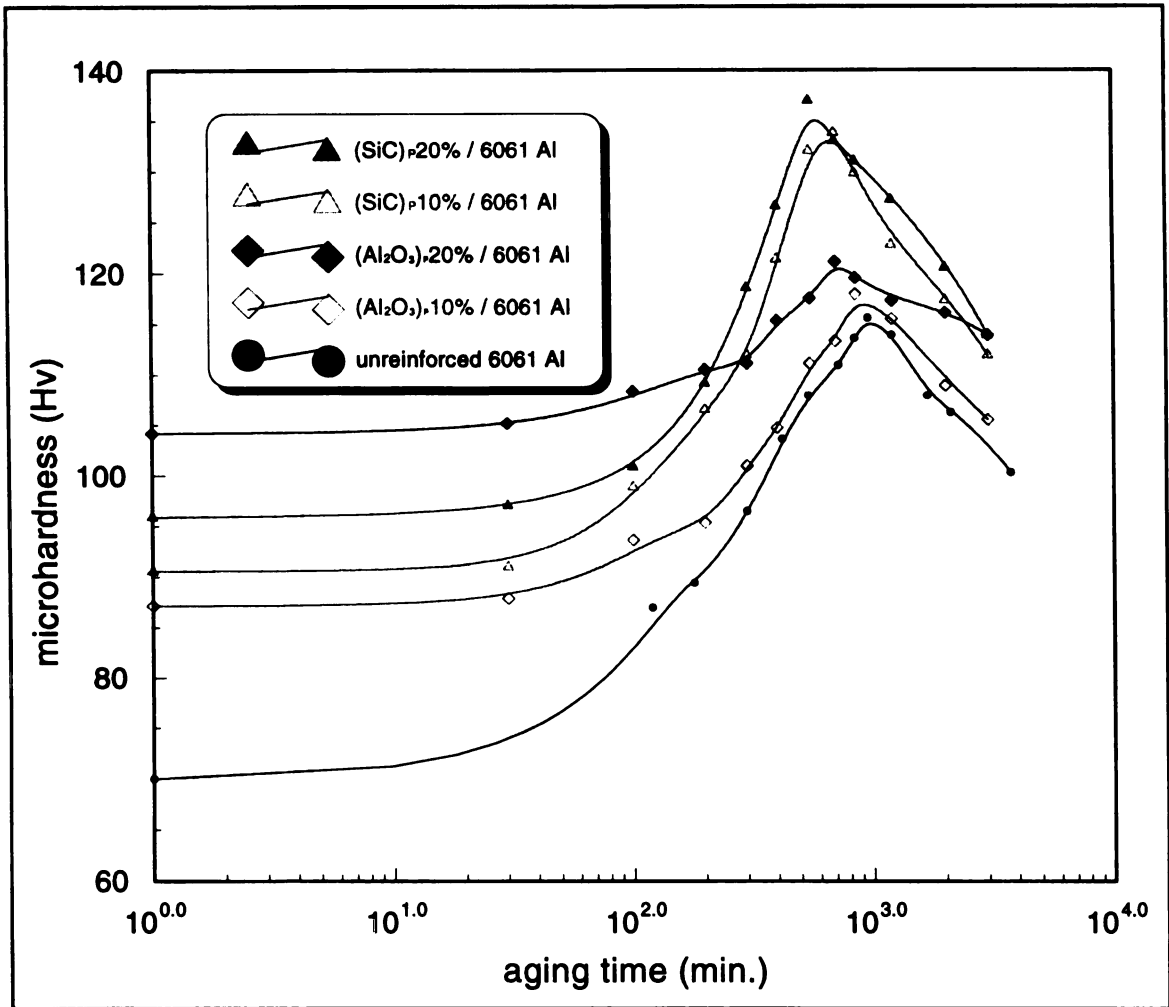


Figure 18. Microhardness variation for several PRMMCs and the complementary unreinforced matrix alloy as a function of aging time (aging temp. 180°C). Accelerated aging is indicated by the curve peaks shifting to the left.

Table 6. Average microhardness values for several PRMMCs during aging. Standard deviation values are in parentheses. (Unit: Hv)

time	10% (Al ₂ O ₃) _p /6061Al	20% (Al ₂ O ₃) _p /6061Al	10% SiC _p /6061Al	20% SiC _p /6061Al
1	87.1 (1.3)	104.2 (3.3)	90.6 (3.2)	95.9 (2.6)
30	87.9 (1.2)	105.2 (1.9)	91.0 (0.7)	97.0 (3.2)
100	93.6 (1.6)	108.4 (2.1)	98.9 (2.5)	100.9 (2.5)
200	95.3 (2.4)	110.6 (2.2)	106.6 (2.6)	109.2 (1.9)
300	101.0 (2.0)	111.2 (1.9)	110.0 (2.2)	118.6 (3.6)
400	104.8 (1.9)	115.4 (1.1)	121.4 (2.3)	126.6 (2.6)
550	111.2 (2.9)	117.6 (1.1)	132.0 (2.9)	137.0 (3.9)
700	113.4 (2.9)	121.2 (2.2)	133.8 (1.0)	133.0 (1.5)
850	118.0 (2.5)	119.6 (6.3)	129.8 (1.9)	131.0 (2.3)
1200	115.6 (1.9)	117.4 (2.1)	122.8 (1.5)	127.2 (3.7)
2000	109.0 (1.9)	116.2 (2.2)	117.4 (2.6)	120.6 (5.1)
3000	105.6 (4.0)	114.0 (2.5)	112.0 (2.1)	114.0 (2.4)

For similar reinforcement content, the SiC_p reinforced MMCs exhibit significantly higher microhardness values than that of Al_2O_3 reinforced composites in the peak aged condition. The hardness difference can be rationalized by noting the difference in resultant matrix composition due to the different interfacial reactions between Al_2O_3 and SiC reinforced composites. At the Al_2O_3 /6061Al interface, magnesium is consumed and the pure aluminum is rejected during the formation of MgAl_2O_4 according to Equation 4. Since the major matrix strengthening precipitate in 6061Al-T6 is the β phase (Mg_2Si precipitate) [19], the interfacial reaction results in a decrease in matrix strengthening Mg_2Si precipitation near the reinforcement particles due to Mg consumption during formation of the spinel phase. In contrast, aluminum is consumed and silicon is rejected by the formation of Al_4C_3 at the SiC /6061Al interface according to Equation 5. The higher hardness of SiC /6061Al is presumed to be due to the presence of rejected Si particles and the lack of interfacial reactions which consume matrix-hardening alloying elements [33].

3.4 Fracture Behavior

3.4.1 Crack initiation

Crack initiation processes were observed by conducting 4-point bend testing on double notched bar specimens. During loading of a 4-point bend specimen, catastrophic fracture will occur at one of the two notches. The deformation/microfracture state of the other notch, which exists just prior to catastrophic failure occurs, will be preserved. Thus, optical microscope and SEM examinations performed in the vicinity of the notch tip allow crack initiation for fracture to be assessed. Similar studies of crack initiation events using 4-point bend specimens have been carried by Lewandowski *et. al.* [59]. Figure 19 shows the preserved notch tip for UA and OA conditions of 20% $(\text{Al}_2\text{O}_3)_p/6061\text{Al}$ composite specimens. The microstructure of the notch tip of the UA specimen after bend testing is depicted in Figure 19b. Extensive plastic deformation is seen around the notch tip, at fractured particles, and at the sharp edges of the particles which foster high stress concentration. Figure 20a shows the magnified image of the notch tip area in Figure 19b. The arrows in Figure 20a indicate the fractured particles around the notch tip and the tendency for void initiation at sharp edges of the reinforcements. By comparison, the preserved notch tip region of the OA specimen (Figure 19d) revealed no observable crack initiation and/or microfracture events. Void growth and microcrack link-up occur by the matrix failure. No significant damage initiation at the preserved notch tip in the OA condition suggests that no time lag between microcrack and catastrophic main crack propagation. This type of crack initiation and fracture behavior typify materials which possess low fracture toughness, tensile ductility and strain to fracture (ϵ_f).

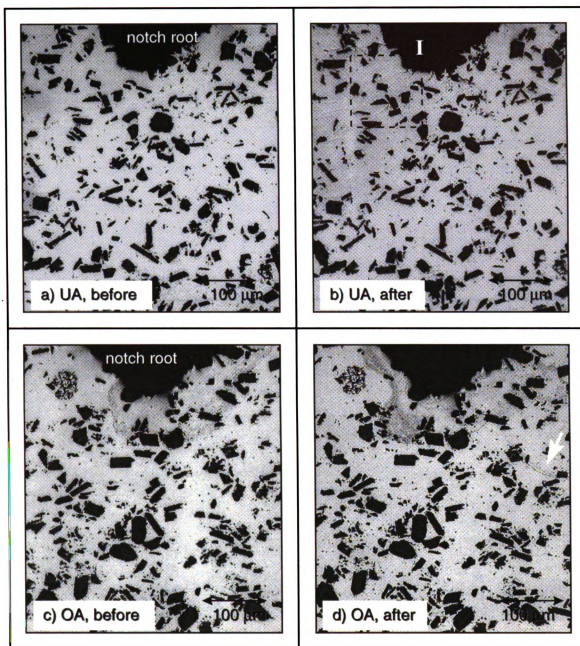


Figure 19. Observation of crack initiation processes in 20% (Al_2O_3)/6061Al composite by conducting 4-point bend testing on double-notched bar specimens, a) before the test (UA), b) after the test (UA) showing extensive plastic deformation around the notch tip (a magnified view(5 \times) of area I is shown in Figure 20), c) before the test (OA), d) after the test (OA), the arrows indicating the void nucleation at the reinforcements and link up by matrix failure.

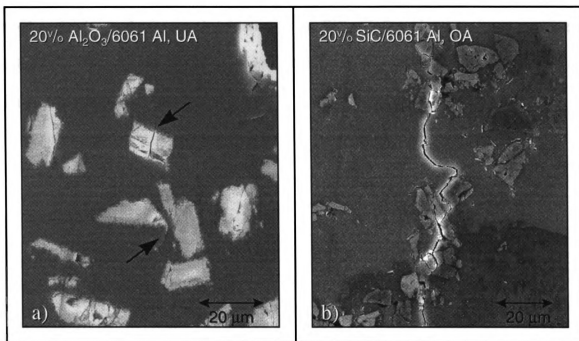


Figure 20. Magnified images of notch tip area in PRMMCs from post-tested 4-point bend bar specimens, a) magnified image from Figure 19b, arrows indicating fractured particles around the notch tip and tendency for void initiation at sharp edges of the reinforcements, b) magnified image from Figure 21d showing preferential crack propagation path through SiC_p cluster regions and SiC_p clusters link up via matrix failure.

Aspects of crack initiation behavior at the notch tip for UA and OA, 20% SiC_p/6061Al are shown in Figure 21. Crack initiation occurs at the SiC_p/matrix interface for the UA specimen (Figure 21b). Similarly in OA condition, microfracture preferentially occurs at the SiC_p/matrix interface fracture. Also, the crack propagation path tended to seek out SiC_p cluster regions. As is common with other materials, microcracks associated with SiC_p clusters link up via matrix failure (Figure 20b and 21d). It was quite apparent that preferential crack initiation favored the SiC_p/matrix interface and SiC_p clusters regardless of the aging condition or reinforcement content. Preferential void nucleation and microcrack initiation in the SiC_p reinforced composite is seemingly influenced by the weak bonding strength of SiC_p/matrix interface due to formation of interfacial Al₄C₃.

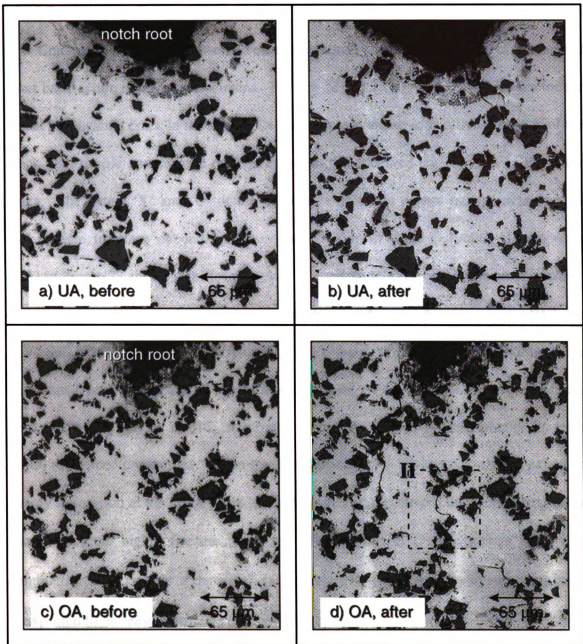


Figure 21. Observation of crack initiation processes in 20% SiC_p/6061Al composite by conducting 4-point bend testing on double-notched bar specimens, a) before the test (UA), b) after the test (UA) showing preferential crack initiation at the interface of the particles, c) before the test (OA), d) after the test (OA) showing preferential crack propagation through SiC_p cluster regions, and link up of the microcracks by matrix failure (a magnified view(5×) of area II is shown in Figure 20).

3.4.2 Crack propagation

Crack propagation was observed on the sectioned and polished halves of post-tested short bar fracture toughness specimens. Figures 22 and 23 show the SEM images for the actual propagating crack in the PRMMCs and a corresponding illustrative drawings of the crack path profile and damage enclave consisting of fractured particles left in the crack wake. The letters 'X' and 'O' of the illustrative drawings denote transparticle fracture and particle interface debonding, respectively. The 20% (Al₂O₃)_p/6061Al composite (UA) in Figure 22 shows significant amount of transparticle fracture in the crack enclave, and in this case, particle fracture dominated the microfracture process. In contrast, for 20% SiC_p/6061Al composite (UA) in Figure 23 shows that interface debonding is the dominant fracture mechanism. In addition, the size of the damage enclave associated with crack propagation in SiC_p reinforced composite is considerably smaller than for Al₂O₃ reinforced composites. Since the damage enclave is associated with the extent of energy absorption at the crack tip, a wider damage enclave around the propagating crack should promote higher fracture toughness. Also, the size of the damage enclave is commensurate to the size of the crack tip process zone (l^*). Thus, the fracture toughness is expected to increase with l^* as following equation [52,62]:

$$G_c = \frac{K_c^2}{E} = \alpha^* \varepsilon_f^* \sigma_o l^* . \quad (7)$$

Where G_c is fracture energy of a composite, K_c is critical stress intensity factor, E is elastic modulus of a composite, α^* is constant, ε_f^* is stress-modified fracture strain, and σ_o is composite strength.

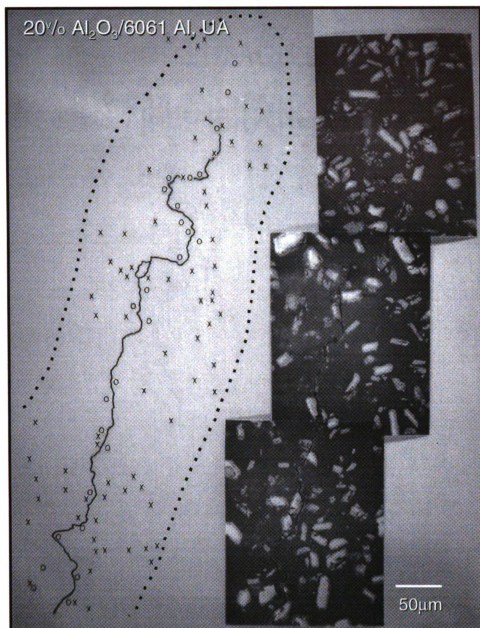


Figure 22. SEM images of the actual crack propagation in 20% $(\text{Al}_2\text{O}_3)_p/6061\text{Al}$ composite (UA) and a corresponding illustrative drawings of the crack path profile and damage enclave (indicated by dashed lines) consisting of fractured particles left in the crack wake (note that 'X' = transparticle fracture, and 'O' = interface debonding).

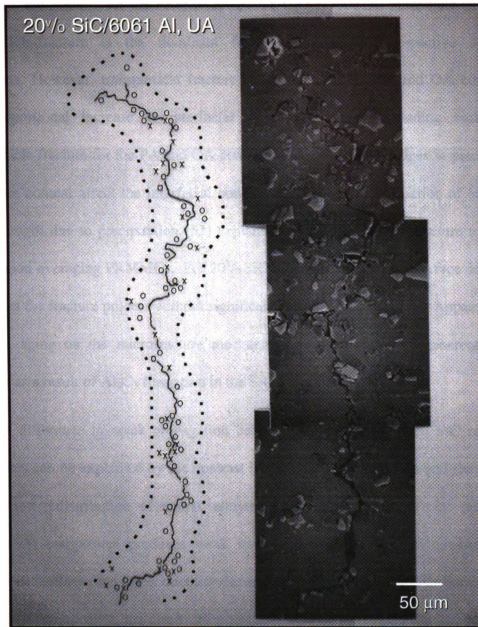


Figure 23. SEM images of the actual crack propagation in 20% SiC_p/6061Al composite (UA) and a corresponding illustrative drawings of the crack path profile and damage enclave (indicated by dashed lines) consisting fractured particles left in the crack wake (note that 'X'= transparticle fracture, and 'O'= interface debonding), a) 20% (Al₂O₃)_p/6061Al composite (UA), b) 20% SiC_p/6061Al composite (UA).

The effect of aging on fracture mechanisms along the crack path is exhibited in Figure 24 and Table 7 for the PRMMCs. 20% $(\text{Al}_2\text{O}_3)_p$ /6061Al composite shows that transparticle-fracture is the dominant fracture mechanism irrespective of aging conditions. However, transparticle fracture is slightly less for PA and OA conditions. The proportional increase in interfacial debonding or corresponding decrease in transparticle fracture for the PA and OA conditions suggests that changes in precipitation and phase content affect the interfacial bonding strength [59]. Reduction of interfacial bond strength due to precipitation [53] explains why no recovery in fracture toughness occurs upon overaging PRMMCs. For 20% SiC_p /6061Al composite, interface debonding dominates the fracture process without significant variation due to aging. Apparently, the effect of aging on the microfracture mechanisms is masked by the inherently weak interface as a result of Al_4C_3 formation in the SiC_p reinforced composites.

The difference in crack propagation behavior between Al_2O_3 and SiC reinforced composites can be explained by the contrast in the interfacial reactions and the resultant composition redistribution of matrix alloying elements. The interfacial reaction in SiC_p /6061Al composites produces weak interfacial bonding strength combined with higher peak hardness and lower ductility due to the alloying element redistribution. In the SiC_p /6061Al composites, the crack can propagate without significant damage around the crack tip due to the low load transfer efficiency at the weak interface and low fracture toughness of the matrix. However, extensive particle fracture in the crack wake occurred for $(\text{Al}_2\text{O}_3)_p$ /6061Al composites, which suggested that the interfacial strength was considerably higher.

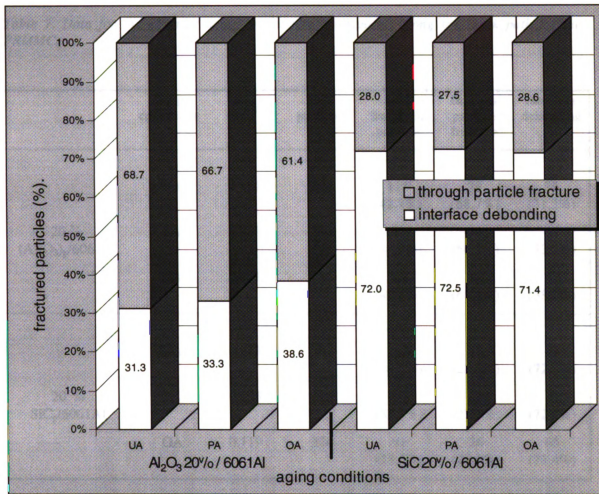


Figure 24. Effect of aging on fracture mechanisms along the crack path for the PRMMCs. 20% (Al₂O₃)/6061Al composite shows the transparticle fracture as dominant fracture mechanism irrespective of aging conditions. 20% SiC/6061Al composite shows the interface debonding as dominant fracture mode without significant variation due to aging.

Table 7. Data for the effect of aging on fracture mechanisms along the crack path for the PRMMCs.

	aging conditions	area (mm ²)	total particles	total fractured particle	through particle fracture	interface debonding
20 % (Al ₂ O ₃) _p /6061Al	UA	0.157	269	115 (42.7%)	79 (68.7%)	36 (31.3%)
	PA	0.155	230	99 (43.0%)	66 (66.7%)	33 (33.3%)
	OA	0.151	236	101 (42.8%)	62 (61.4%)	39 (38.6%)
20 % SiC _p /6061Al	UA	0.103	362	132 (36.5%)	37 (28.0%)	95 (72.0%)
	PA	0.110	275	102 (37.1%)	33 (27.5%)	87 (72.5%)
	OA	0.119	274	91 (33.2%)	26 (28.6%)	65 (71.4%)

The SEM micrographs in Figure 25 show fracture of the crack tip area of the PRMMCs. In Figure 25, the OA 20% (Al₂O₃)_p/6061Al composite exhibits the extensive particle cracking around the crack tip, while the PA 20% SiC_p/6061Al composite shows the fractured particles only at the crack path and no significant damage around the crack tip. Also, Figure 25b shows preferential crack propagation through SiC particulate clustered regions and microcrack link up between the particulate clusters. Microcracks that nucleated at SiC_p clusters ahead of the crack tip grew in the composite material and linked up with the main crack to sustain crack propagation. The SEM fractographs in Figure 26 show typical fracture behavior of the particles in 20% (Al₂O₃)_p/6061Al (OA). Figure 26a shows the morphology of the fracture surface which exhibits transparticulate dominant fracture mechanism. Figure 26b shows cracked Al₂O₃ particles on the fracture surface and Figure 26c shows transparticulate fractured particle with interface debonding. The typical transparticulate fracture of an Al₂O₃ particle is shown in Figure 26d, and void growth around the (Al₂O₃)_p is quite evident. This type of microcrack nucleation by particulate cracking tends to impede void coalescence by constraining plastic flow in the matrix, thus leading to reduced ductility and fracture toughness [53]. The SEM fractographs in Figure 27 show typical fracture behavior of the particles in 20% SiC_p/6061Al (OA). Figure 27a shows the morphology of the fracture surface which exhibits interface debonding-dominant fracture mechanism. At higher magnification, Figure 27b shows interface debonded SiC particles on the fracture surface and Figure 27c shows the transparticulate fracture. Figure 27d shows the typical interface debonded SiC_p in the particle in 20% SiC_p/6061Al composite. Debonded SiC particles are abundantly found on fracture surface for all aging conditions indicating that the interfacial debonding was the dominant microfracture mechanism.

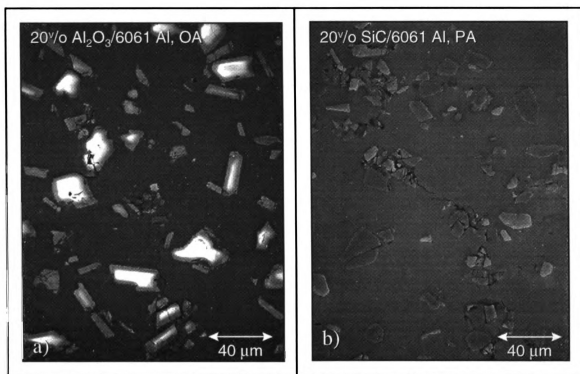


Figure 25. SEM micrographs showing the crack tip of the PRMMCs, a) crack tip of 20% (Al_2O_3)/6061Al composite(OA) showing the extensive particle cracking around the crack tip, b) 20% SiC/6061Al composite (PA) showing preferential crack propagation through SiC particulate clustered region and microcrack link up between the particulate clusters.

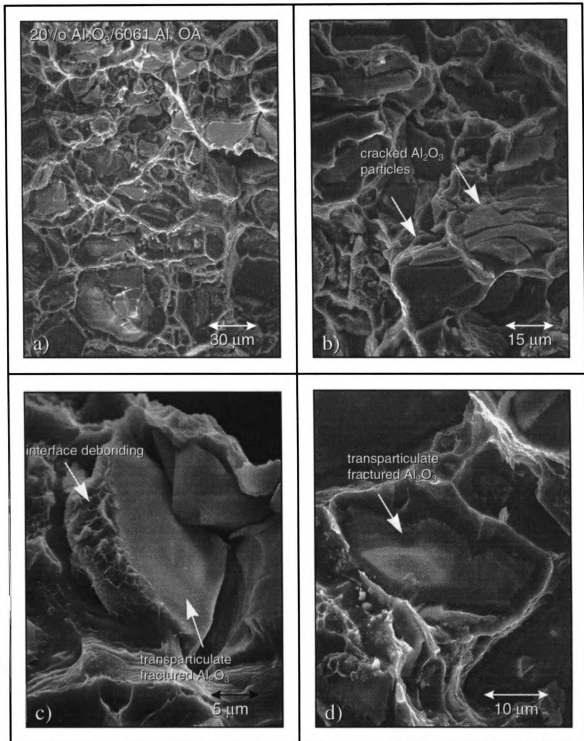


Figure 26. SEM fractography of 20% (Al₂O₃)/6061Al composite(OA), a) morphology of fracture surface, b) cracked Al₂O₃ particles, c) both transparticle fractured and interface debonded Al₂O₃ particle, d) transparticle fractured Al₂O₃ particle.

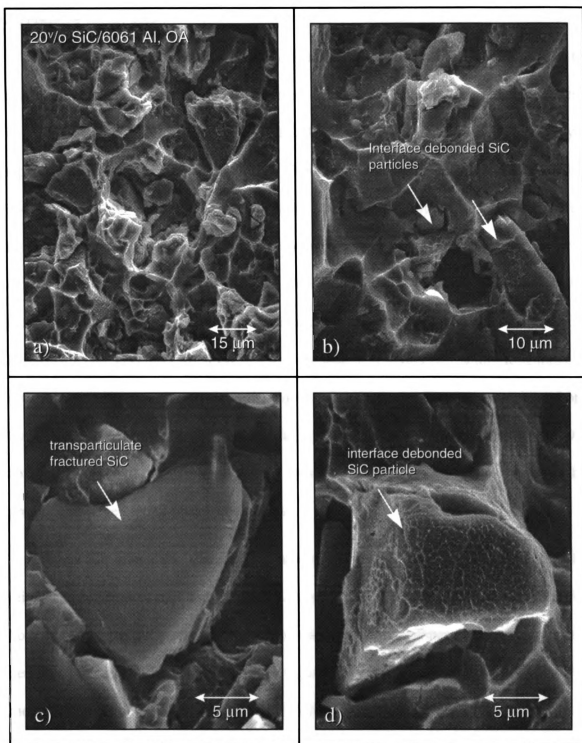


Figure 27. SEM fractography of 20% SiC/6061Al composite(OA), a) morphology of fracture surface, b) interface debonded SiC particles, c) transparticulate fractured SiC particle, d) interface debonded SiC particle.

3.5 Fracture Toughness

Figure 28 and Table 8 show the comparison of the fracture toughness (K_{Ic}) relative to aging time. None of the composite materials exhibited recovery of fracture toughness with aging. The fracture toughness of PRMMCs, unlike unreinforced matrix alloys, typically do not recover on overaging [50,53,56,59]. Manoharan and Lewandowski [53] observed that the toughness decrease between UA and OA composite materials was due to the transition in the local fracture mode from SiC particle cracking to SiC/matrix near interface debonding. Increased interface debonding in OA condition was due to the precipitation at SiC_p/matrix interface that reduced the interfacial bond strength [53]. Klimowicz and Vecchio [56] suggested that the lack of recovery of fracture toughness of over aged MMCs was due to the strain localization in matrix ligaments resulting from fracture of the reinforcement particles. The ligaments showed premature fracture in OA condition as secondary microvoids readily formed within the matrix ligaments due to the presence of large second-phase precipitates.

Figure 28 illustrates that the fracture toughness decreases significantly as the reinforcement content and aging time (i.e. increased hardness and strength) increase for both (Al₂O₃)_p and SiC_p reinforced composites. Fracture toughness for crack initiation decreased linearly with the increase in the volume fraction of the reinforcement [53]. For the UA condition, Al₂O₃ reinforced PRMMCs show considerably higher fracture toughness values than that of SiC reinforced composites. However, the difference of the fracture toughness values between Al₂O₃ and SiC reinforced composites is noticeably less in the PA and OA conditions. This difference in fracture toughness behavior as a result of aging can be rationalized as follows. The low fracture toughness of SiC reinforced

composites in UA condition is due to the weak interfacial bonding strength resulting in low load transfer efficiency. Considerably stronger interfacial bonding strength in Al_2O_3 reinforced composites in the UA condition results in more efficient load transfer in the ductile matrix, thus contributing to higher fracture toughness. With increasing aging time, at the PA and OA conditions, the fracture toughness of the Al_2O_3 reinforced composites decreases due to the reduction of the matrix ductility and weakening of the interface. For SiC reinforced composites, aging effects on fracture toughness are reduced by the weak interfacial bonding strength resulting in smaller variation of the fracture toughness upon aging.

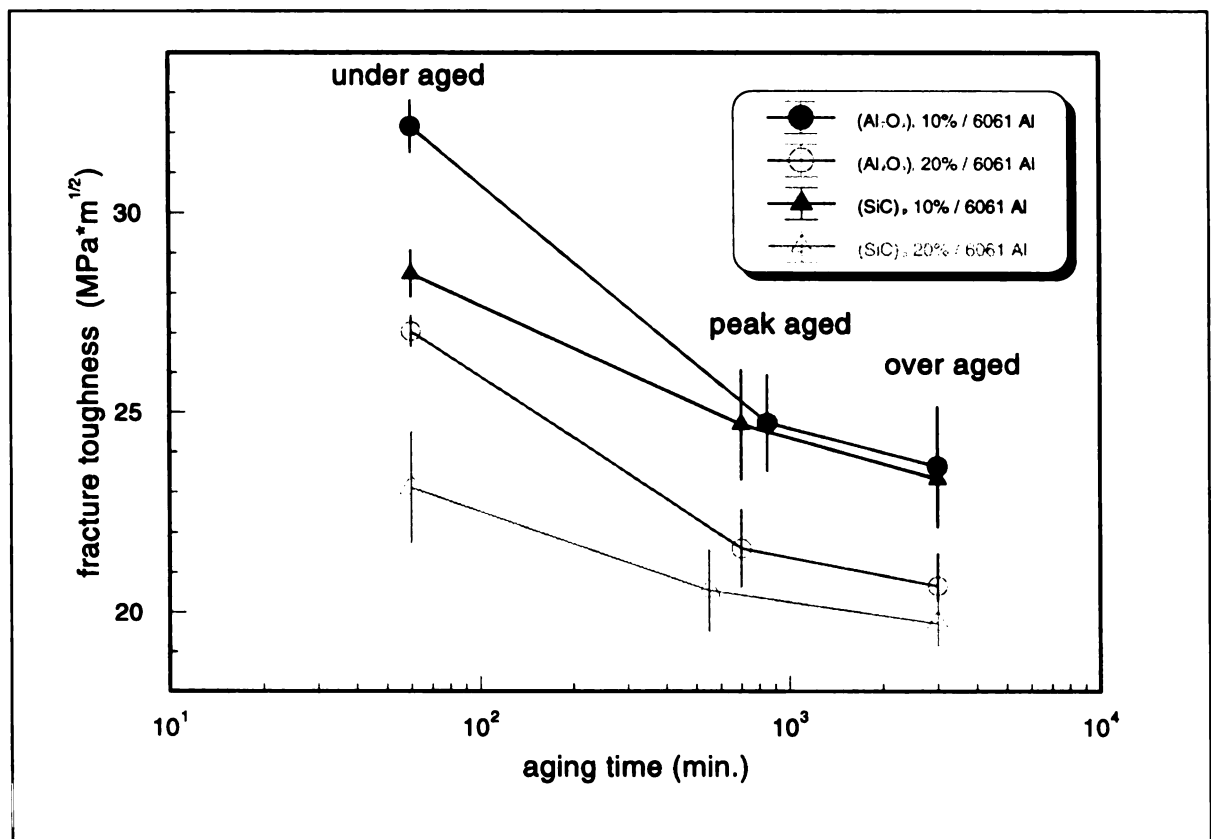


Figure 28. Comparison of fracture toughness (K_q) variation for the PRMMCs as a function of aging time (three specimens were tested to obtain each datum point).

Table 8. Fracture toughness(K_q) values for the various PRMMCs as a function of aging conditions. (Unit: $\text{MPa}\sqrt{\text{m}}$, unit of values in parentheses: $\text{Ksi}\sqrt{\text{in}}$)

	UA	PA	OA
10% (Al₂O₃)_p/6061Al	31.36 (28.53)	22.83 (20.77)	22.60 (20.56)
	32.40 (29.48)	25.77 (23.45)	23.35 (21.25)
	32.70 (29.75)	23.15 (21.06)	21.98 (20.00)
average	29.25 (32.15)	21.76 (23.91)	20.61 (22.65)
standard deviation	0.64 (0.70)	1.47 (1.62)	0.63 (0.69)
20% (Al₂O₃)_p/6061Al	27.45 (24.98)	20.52 (18.67)	19.99 (18.19)
	27.04 (24.60)	21.66 (19.71)	21.67 (19.72)
	26.62 (24.22)	22.62 (20.58)	20.30 (18.47)
average	24.60 (27.04)	19.65 (21.60)	18.79 (20.65)
standard deviation	0.38 (0.42)	0.96 (1.05)	0.81 (0.90)
10% SiC_p/6061Al	28.41 (25.85)	25.98 (23.64)	23.56 (21.44)
	27.88 (25.37)	23.04 (20.96)	23.98 (21.82)
	29.15 (26.52)	25.04 (22.78)	22.41 (20.39)
average	25.91 (28.48)	22.46 (24.68)	21.22 (23.32)
standard deviation	0.58 (0.63)	1.37 (1.50)	0.74 (0.81)
20% SiC_p/6061Al	23.99 (21.83)	20.73 (18.86)	19.35 (17.61)
	21.35 (19.43)	21.56 (19.62)	20.41 (18.57)
	23.99 (21.83)	19.35 (17.61)	19.35 (17.61)
average	21.03 (23.11)	18.70 (20.55)	17.93 (19.71)
standard deviation	1.39 (1.52)	1.01 (1.12)	0.55 (0.61)

Chapter IV

CONCLUSIONS

- Accelerated aging is observed for all of the particulate reinforced metal matrix composites. Higher hardness values were observed with higher V_f regardless of the type, however, SiC_p MMCs exhibited significantly higher hardness than Al_2O_3 composites in the peak aged condition.
- The major interfacial reaction products found were MgAl_2O_4 for $(\text{Al}_2\text{O}_3)_p/6061\text{Al}$ composites and Al_4C_3 for $\text{SiC}_p/6061\text{Al}$ composites. Coverage of alumina particulates with octahedral-shaped spinel (MgAl_2O_4) crystals ($\sim 1 \mu\text{m}$) is nearly 100%. A significant amount of Al_4C_3 was found at the reinforcement/matrix interface. The morphology of the reaction product, Al_4C_3 , was a hexagonal platelet shape resulting in decrease of interfacial bonding strength. The instability of the Al_4C_3 phase was clearly exhibited as dissolution occurred when these crystals are in direct contact with water. ESEM images showed that the disintegration of Al_4C_3 occurred in less than 120 h when exposed to a moisture environment.
- Preferential crack initiation occurred at the SiC_p /matrix interface and near SiC_p clusters regardless of the aging condition or reinforcement content. Preferential interfacial fracture of the SiC_p composite is promoted by the weak SiC_p /matrix interface bonding strength due to Al_4C_3 formation. In contrast, transparticle fracture was the dominant fracture mechanism for $(\text{Al}_2\text{O}_3)_p/6061\text{Al}$ composites irrespective of

aging conditions, as the $\text{MgAl}_2\text{O}_4/(\text{Al}_2\text{O}_3)_p$ interface is strong in comparison to the $\text{SiC}_p/\text{Al}_4\text{C}_3$ interface.

- The fracture toughness decreased with aging time, and no recovery of the fracture toughness was observed with over aging. $(\text{Al}_2\text{O}_3)_p$ MMCs exhibited higher fracture toughness than SiC_p MMCs, when V_f remained constant.
- Post-test examination of fracture toughness specimens revealed extensive fracture in the wake of the propagating crack for $(\text{Al}_2\text{O}_3)_p/6061\text{Al}$ composites. However, substantially less particle cracking was observed in the crack wake for $\text{SiC}_p/6061\text{Al}$ composites, as interfacial debonding was dominant. The damage enclave associated with crack propagation and related to the 'process zone' in the $(\text{Al}_2\text{O}_3)_p/6061\text{Al}$ composite was ~3 times as large as the damage enclave in $\text{SiC}_p/6061\text{Al}$ composite material. The composite material exhibiting a larger enclave revealed higher fracture toughness.

LIST OF REFERENCES

1. M. M. Schwartz, *Composite Materials Hand book*, Heightstown, NJ, McGraw-Hill, (1984) p. 670.
2. D. R. Flinn, *The New Materials society vol. 2*, Bureau of Mines (1990) p. 6-1
3. M. Hunt, "Aluminum Composites Come of Age," *Materials Engineering*, Vol. 106 (1989) p. 37.
4. P. Rohatgi, "Advances in Cast MMCs," *Advanced Materials & Processes*, Vol. 136 (1990) p. 39.
5. S. Caron & J. Masounav, "A literature Review of Fabrication Techniques of Particulate Reinforced Composites, Fabrication of Particulate Reinforced Metal Matrix Composites," Eds. J. Masounave & F. G. Hamel, *AMS Conference Proceedings*, Montréal, Québec, Canada (1990) p. 79.
6. Hideo Ohtsu, "Aluminum Alloys Matrix Composites Using Particle Dispersion, Design & Manufacturing of Advanced Composites," *ASM conference proceedings* (1989) p. 187.
7. M. G. McKimpson & T. E. Scott, "Processing and Properties of Metal Matrix Composites Containing Discontinuous Reinforcement," *Materials Science and Engineering*, Vol. A107 (1989) p. 93
8. B. F. Quigley, G. J. Abbaschin, R. Wunderlin & R. Mehrabian, "A Method for Fabrication of Aluminum-Alumina Composites," *Metallurgical Transactions A*, Vol. 13A (1982) p. 93.
9. F. A. Girot, J. M. Quenisset & R. Naslain, "Discontinuously-Reinforced Aluminum Matrix Composites," *Composite Science and Technology*, Vol. 30 (1987) p. 155.
10. J. R. Davis, *ASM Specialty Handbook; Aluminum and Aluminum alloys*, Materials Park, OH: ASM International (1993) p. 160.
11. T. J. Reinhart, *Engineered Materials Handbook*, ASM, Vol. 1 (1987) p. 904.
12. Duralcan[®] company, *Data Manual*, San Diego, CA: Duralcan[®] (1992).
13. A. L. Geiger & M. Jackson, "Low-Expansion MMCs Boost Avionics," *Advanced Materials & Properties*, Vol. 137 (1989) p. 23.
14. T. J. Reinhart, *Engineered Materials Handbook*, ASM, Vol. 4 (1987) p. 974

15. P. Rohatgi, "Cast Aluminum-Matrix Composites for Automotive Applications," *Journal of Materials*, Vol. 43 (1991) p. 10.
16. John E. Hatch, "Aluminum-properties and Physical Metallurgy," *ASM*, (1984) p. 134
17. Metals Handbook, 10th edition, *ASM International*, Vol. 2 (1990) p. 102
18. W. F. Smith, "The Effect of Reversion of Treatments on Precipitation Mechanisms in an Al-1.35 at. pct Mg₂Si Alloy," *Metallurgical Transactions*, Vol. 4 (1973) p. 2435.
19. H. J. Rack & R. W. Krenzer, "Thermomechanical Treatment of High Purity 6061Aluminum," *Metallurgical Transactions A*, Vol. 8A (1977) p. 335
20. T. G. Nieh & R. F. Karlak, "Aging Characteristics of B₄C-Reinforced 6061-Aluminum," *Scripta Metallurgica*, Vol. 18 (1984) p. 25.
21. M. Vogelsang, R. J. Arsenault & R. M. Fisher, "An *In-situ* HVEM Study of Dislocation Generation at Al/SiC Interface in Metal Matrix Composites," *Metallurgical Transactions A*, Vol. 17A (1986) p. 379.
22. R. J. Arsenault & N. Shi, "Dislocation Generation Due to Difference between the coefficients of Thermal Expansion," *Materials Science and Engineering*, Vol. 81 (1986) p.175.
23. T. Christman & S. Suresh, "Microstructural Development in an Aluminum Alloy-SiC Whisker Composite," *Acta Metallurgica*., Vol. 36 (1988) p. 1691.
24. J. M. Papazian, "Effects of SiC Whiskers and Particles on Precipitation in Aluminum Matrix Composites," *Metallurgical Transactions A*, Vol. 19A (1988) p. 2945.
25. I. Dutta & D. L. Bourell, "Theoretical and Experimental Study of Aluminum Alloy 6061-SiC Metal Matrix Composite to Identify the Operative Mechanism for Accelerated Aging," *Materials Science and Engineering*, Vol. A112 (1989) p. 67.
26. J. J. Stephens, J. P. Lucas & F. M. Hosking, "Cast Al - 7 Si Composites: Effect of Particle type and Size on Mechanical Properties," *Scripta Metallurgica*, Vol. 22 (1988) p. 1307.
27. S. Dionne, M. R. Krishnadev, & R. Bouchard, "Effects of Heat Treatment on the Microstructure and Tensile Properties of a P/M SiC Particulate / 7091 Al MMC," *Metal & Ceramic Matrix Composites: Processing, Modeling & Mechanical Behavior*, Eds. R. B. Bhagat, A. H. Clauer, P. Kumer & A. M. Ritter, TMS (1990).
28. E. Hunt, P. D. Pitcher & P. J. Gregson, "Precipitation Reactions in 8090 SiC Particulate Reinforced MMC," *Scripta Metallurgica*., Vol. 24 (1990) p. 937.

29. K. K. Chawla, A. H. Esmaeili, A. K. Datye & A. K. Vasudevan, "Effect of Homogeneous Precipitation on Aging Behavior of SiC_p / Al 2014 Composite," *Scripta Metallurgica.*, Vol. 25 (1991) p. 1315.
30. P. Appendino, C. Badini, F. Marino & A. Tomasi, "6061 Aluminum alloy-SiC particulate composite: a comparison between aging behavior in T4 and T6 treatments," *Materials Science and Engineering*, Vol. A135 (1991) p. 275
31. H. L. Lee, W. H. Lu & S. L. Chan, "Effect of Cold Rolling on the Aging Kinetics of Al₂O₃ / 6061Al Composite by Differential Scanning Calorimetric Technique," *Scripta Metallurgica*, Vol. 25 (1991) p. 2165
32. I. Dutta, S. M. Allen & J. L. Hafley, "Effect of Reinforcement on the Aging Response of Cast 6061Al-Al₂O₃ Particulate Composite," *Metallurgical Transactions A*, Vol. 22A (1991) p. 2553.
33. L. Salvo, M. Suéry, J. G. Legoux & G. L'Esérance, "Influence of Particle Oxidation on Age-Hardening Behavior of As-Fabricated and Remelted SiC reinforced Al-1% Mg Alloys," *Materials Science and Engineering*, Vol. A135 (1991) p. 129.
34. J. C. Lee, K. N. Subramanian & Y. Kim, "The Interface in Al₂O₃ particulate-reinforced aluminum alloy composite and its role on the tensile properties," *Journal of Materials Science*, Vol. 29 (1994) p. 1983.
35. J. P. Lucas, J. J. Stephens & F. A. Greulich, "The Effect of Reinforcement Stability on Composition Redistribution in Cast Aluminum Metal Matrix Composites," *Materials Science and Engineering*, Vol. A131 (1991) p. 221.
36. S. Suresh, A. Mortensen & A. Needleman, *Fundamentals of Metal Matrix Composites*, Stoneham, MA: Butterworth-Heinemann, (1993) p. 251.
37. T. A. Chernyshova & A. V. Rebrov, "Interaction Kinetics of Boron Carbide and Silicon Carbide with Liquid Aluminum," *Journal of the Less-Common Metals*, Vol. 117 (1986) p. 203.
38. D. J. Lloyd, H. Lagace, A. McLeod & P. L. Morris, "Microstructural Aspects of Aluminum-Silicon Carbide Particulate Composites Produced by a Casting Method," *Materials Science and Engineering*, Vol. A107 (1989) p. 73.
39. G. Gonzalez, L. Salvo, M. Suéry & G. L'Esérance, "Interfacial Reactions In Al-Mg Metal Matrix Composites Reinforced with (Sn/Sb) Oxide Coated SiC Particles," *Scripta Metallurgica.*, Vol. 33 (1995) p. 1969.

40. H. Ribes, M. Suéry, G. L'Esérance & J. G. Legoux, "Microscopic Examination of the Interface Region in 6061-Al/SiC Composites Reinforced with As-Received and Oxidized SiC Particles," *Metallurgical Transactions A*, Vol. 21A (1990) p. 2489.
41. J. C. Lee, J. I. Lee & H. I. Lee, "Observation of Interfacial Reaction in SiC_p / Al composites and their characterizations," *In press*.
42. T. Iseki, T. Kameda & T. Maruyama, "Interfacial Reactions between SiC and Aluminum during Joining," *Journal of Materials Science*, Vol. 19 (1984) p. 1962.
43. Ray Y, Lin, Sunil G. Warriar, Shyi K. Wu & Jein Y. Wang, "Infrared Aluminum Matrix Composites and Carbide Formation," *Proceeding of ICCM-10*, Whistler, B.C., Canada, August 1995, Vol II : Metal Matrix Composites, p. II-271.
44. L. N. Thanh & M. Suéry, "Influence of Oxide Coating on Chemical Stability of SiC Particles in Liquid Aluminum," *Scripta Metallurgica.*, Vol. 25 (1991) p. 2781.
45. A. Munitz, M. Metzger & R. Mehrabian, "The Interface Phase in Al-Mg/Al₂O₃ Composites," *Metallurgical Transactions A*, Vol. 10A (1979) p. 1491.
46. J. C. Lee, G. H. Kim, J. I. Lee & H. I. Lee, "Characterization of Interfacial Reaction in (Al₂O₃)_p/6061Al Composite," *In press*.
47. R. Molins, J. K. Bartout and Y. Bienvenu, "Microstructural and Analytical Characterization of Al₂O₃-(Al-Mg) Composite Interfaces," *Materials Science and Engineering*, Vol. A135 (1991) p. 111.
48. B. F. Quigely, G. J. Abbaschina, R. Wunderlin & R. Mehrabian, "A Method for Fabrication of Aluminum-Alumina Composites," *Metallurgical Transactions A*, Vol. 13A (1982) p. 93
49. C. P. You, A. W. Thompson & I. M. Bernstein, "Proposed Failure Mechanism in a Discontinuously Reinforced Aluminum Alloy," *Scripta Metallurgica.*, Vol. 21 (1987) p. 181..
50. D. J. Lloyd, "Aspects of Fracture in Particulate Reinforced Metal Matrix Composites," *Acta Metallurgica.*, Vol. 39 (1991) p. 59.
51. D. L. Davison, "Fracture Characteristics of Al-4 Pct Mg Mechanically Alloyed with SiC," *Metallurgical Transactions A*, Vol. 18A (1987) p. 2115.
52. J. P. Lucas, P. K. Liaw, J. J. Stephens & J. Nunes, "The Effect of Particulate Fracture in Determining Fracture Toughness of Metal Matrix Composites," *Proceedings of*

- Morris E. Fine Symposium*, Eds. P. K. Liaw, J. R. Weertman, H. L. Marcus & J. S. Santner, TMS (1991) p. 171.
53. M. Manoharan & J. J. Lewandowski, "Crack Initiation and Growth Toughness of an Aluminum Metal-Matrix Composite," *Acta Metallurgica.*, Vol. 38 (1990) p. 489.
 54. M. Manoharan & J. J. Lewandowski, "*In-situ* Deformation Studies of an Aluminum Metal-Marix Composite in a Scanning Electron Microscope," *Scripta Metallurgica.*, Vol. 23 (1989) p. 1801.
 55. S. V. Nair, J. K. Tien & R. C. Bates, "SiC Reinforced Aluminum Metal Matrix Composites," *International Metals Reviews*, Vol. 30 (1985) p. 275.
 56. T. F. Klimowicz & K. S. Vecchio, "The Influence of Aging Condition on the Fracture Toughness of Alumina-Reinforced Aluminum Composites," *Fundamental Relationships Between Microstructure & Mechanical Properties of Metal-Matrix Composites*, Eds. P. K. Liaw & M. N. Gungor, TMS (1990) p. 255.
 57. P. M. Mummery, B. Derby & C. B. Scruby, "Acoustic Emission from Particulate-Reinforced Metal Matrix Composites," *Acta Metallurgica.*, Vol. 41 (1993) p. 1431.
 58. J. Yang, C. Cady, M. S. Hu, F. Zok, R. Mehrabian & A. G. Evans, "Effect of Damage on the Flow Strength and Ductility of Ductile Al Alloy Reinforced with SiC Particulates," *Acta Metallurgica.*, Vol. 38 (1990) p. 2613.
 59. J. J. Lewandowski, C. Liu & W. H. Hunt Jr., *Powder Metallurgy Composites*, Eds. M. Kumar, A. Ritter & K. Vedula, TMS-AIME, Warrendale, PA (1988) p. 117.
 60. W. A. Logsdon & P. K. Liaw, "Tensile, Fracture Toughness and Fatigue Crack Growth Rate Properties of Silicon Carbide Whisker and Particulate Reinforced Aluminum Metal Matrix Composites," *Engineering Fracture Mechanics*, Vol. 24 (1986) p. 737.
 61. Y. Flom & R. J. Arsenault, "Effect of Particle Size on Fracture Toughness of SiC/Al Composite Material," *Acta Metallurgica.*, Vol. 37 (1989) p. 2413.
 62. R.O. Ritchie & A. W. Thompson, "On Macroscopic and Microscopic Analyses for Crack Initiation and Crack Growth Toughness in Ductile Alloys," *Metallurgical Transactions A*, Vol. 16A (1985) p. 233.

APPENDIX

Microhardness values for several PRMMCs during aging. (Unit: Hv)

	*A.R.	*S.T.	30	100	200	300	400	550	700	850	1200	2000	3000
10 % $(\text{Al}_2\text{O}_3)_p$ /6061Al	43.1	89.2	88.4	93.9	93.3	98.9	106.0	111.0	114.0	120.0	115.0	107.0	102.0
	41.4	86.4	88.4	96.2	93.3	102.0	102.0	109.0	111.0	115.0	117.0	111.0	106.0
	43.1	86.1	86.9	92.4	94.5	100.0	107.0	108.0	113.0	118.0	118.0	108.0	101.0
	45.9	86.3	86.4	92.4	98.9	104.0	104.0	113.0	118.0	116.0	113.0	108.0	110.0
	45.4	87.6	89.4	93.3	96.6	100.0	105.0	115.0	111.0	121.0	115.0	111.0	109.0
Average	43.8	87.1	87.9	93.6	95.3	101.0	104.8	111.2	113.4	118.0	115.6	109.0	105.6
St. Dev.	1.9	1.3	1.2	1.6	2.4	2.0	1.9	2.9	2.9	2.5	1.9	1.9	4.0
20 % $(\text{Al}_2\text{O}_3)_p$ /6061Al	70.7	98.9	108.0	110.0	114.0	111.0	115.0	117.0	120.0	126.0	116.0	115.0	115.0
	72.9	106.0	104.0	107.0	111.0	109.0	116.0	118.0	120.0	122.0	119.0	119.0	114.0
	70.7	103.0	106.0	108.0	110.0	112.0	117.0	119.0	125.0	120.0	117.0	114.0	110.0
	65.0	107.0	103.0	111.0	108.0	114.0	114.0	116.0	120.0	121.0	120.0	118.0	117.0
	68.6	106.0	105.0	106.0	110.0	110.0	115.0	118.0	121.0	109.0	115.0	115.0	114.0
Average	69.6	104.2	105.2	108.4	110.6	111.2	115.4	117.6	121.2	119.6	117.4	116.2	114.0
St. Dev.	3.0	3.3	1.9	2.1	2.2	1.9	1.1	1.1	2.2	6.3	2.1	2.2	2.5
10 % SiC _p /6061Al	53.6	90.7	89.2	100.0	106.0	109.0	117.0	131.0	134.0	130.0	119.0	120.0	112.0
	49.0	89.4	92.0	101.0	107.0	114.0	122.0	133.0	132.0	128.0	122.0	115.0	114.0
	50.0	90.7	89.6	98.8	104.0	108.0	121.0	131.0	137.0	132.0	123.0	117.0	111.0
	52.5	90.7	89.2	94.5	106.0	109.0	125.0	133.0	133.0	130.0	124.0	119.0	106.0
	57.2	91.3	94.9	100.0	110.0	110.0	122.0	132.0	133.0	129.0	126.0	116.0	117.0
Average	52.5	90.6	91.0	98.9	106.6	110.0	121.4	132.0	133.8	129.8	122.8	117.4	112.0
St. Dev.	3.2	0.7	2.5	2.6	2.2	2.3	2.9	1.0	1.9	1.5	2.6	2.1	4.1
20 % SiC _p /6061Al	64.8	96.6	101.0	103.0	110.0	127.0	123.0	138.0	132.0	126.0	125.0	113.0	113.0
	57.9	92.4	92.8	98.0	111.0	123.0	126.0	142.0	129.0	130.0	127.0	118.0	109.0
	66.1	94.0	98.0	104.0	106.0	120.0	130.0	137.0	132.0	127.0	131.0	123.0	113.0
	67.7	98.4	94.9	99.3	109.0	118.0	128.0	131.0	132.0	125.0	121.0	123.0	110.0
	67.5	98.0	98.4	100.0	110.0	125.0	126.0	137.0	133.0	130.0	128.0	126.0	115.0
Average	64.8	95.9	97.0	100.9	109.2	122.6	126.6	137.0	131.6	127.6	126.4	120.6	112.0
St. Dev.	4.0	2.6	3.2	2.5	1.9	3.6	2.6	3.9	1.5	2.3	3.7	5.1	2.4

*A.R.→ As Received, S.T.→ Solution Treated, St. Dev. → Standard Deviation.

MICHIGAN STATE UNIV. LIBRARIES



31293015610904